

# 1S-DAug: One-Shot Data Augmentation for Robust Few-Shot Generalization

Yunwei Bai<sup>1</sup> Ying Kiat Tan<sup>1</sup> Yao Shu<sup>2</sup> Tsuhan Chen<sup>1</sup>

## Abstract

Few-shot learning (FSL) challenges model generalization to novel classes based on just a few shots of labeled examples, a testbed where traditional test-time augmentations fail to be effective. We introduce 1S-DAug, a one-shot generative augmentation operator that synthesizes diverse yet faithful variants from just one example image at test time. 1S-DAug couples traditional geometric perturbations with controlled noise injection and a denoising diffusion process conditioned on the original image. The generated images are then encoded and aggregated, alongside the original image, into a combined representation for more robust FSL predictions. Integrated as a training-free model-agnostic plugin, 1S-DAug consistently improves FSL across standard benchmarks of 4 different datasets without any model parameter update, including achieving over 10% proportional accuracy improvement on the miniImagenet 5-way-1-shot benchmark. Codes will be released.

## 1. Introduction

Few-shot learning (FSL) is important for recognition systems deployed in the wild. While deep learning attains strong performance given abundant supervision, their accuracy degrades in rare-case generalization (Wang et al., 2020). Real-world data are long-tailed; rare categories with limited labels persist and cap overall system performance even as head classes continue to grow (Kang et al., 2020). Scarcity in the target domain induces a train-test gap that manifests as high generalization error on novel classes at test time (Wang et al., 2020). As both a testbed and a concrete instance of this long-tail problem, the FSL model must assign labels to previously unseen classes using only a handful of labeled examples per class (Vinyals et al., 2016; Snell et al., 2017). This low-data regime appears in practical settings such as medical imaging for rare diseases and autonomous driving

<sup>1</sup>National University of Singapore <sup>2</sup>Hong Kong University of Science and Technology (Guangzhou). Correspondence to: Yunwei Bai <baiyunwei@u.nus.edu>.

Preprint. February 3, 2026.

with open-world, unpredictable events (Liu & Feng, 2024). The central challenge is to achieve robust generalization under label scarcity and distribution shift.

Data augmentation offers a natural handle on this challenge (Dvornik et al., 2019; Zhou, 2012). From an ensemble perspective, test-time augmentation aggregates predictions across multiple views of the same input and averages out error; in an idealized independence thought experiment, a single-view error rate  $\varepsilon$  would combine as  $\varepsilon^m$  for  $m$  views, while in practice correlation attenuates but does not eliminate the benefit (Zhou, 2012). From a margin perspective, classical generalization bounds can relate test error to data radius; augmentations that contract effective data radii can lower the Rademacher complexity and tighten such bounds (Bartlett & Mendelson, 2002; Bai et al., 2025). On the training side, augmentation increases observed data amount and can tighten the generalization bound further (Hariharan & Girshick, 2017b; Schwartz et al., 2018).

However, the augmentation is effective only with both diversity and accuracy (Zhou, 2012). Standard geometric or photometric transforms like cropping, resizing and scaling often add limited new information and may degrade image quality (Bai et al., 2025). In FSL, where each example carries high influence, degradations are especially harmful at test time, and the model must rely on precise visual cues. Achieving high diversity while preserving class-defining content is therefore central.

Generative data augmentation has potential, but deploying it under FSL constraints is nontrivial. Image-to-image translation with adversarial training (e.g., FUNIT, CycleGAN) can be effective in specific domains, yet it is prone to training instabilities and to inconsistent quality across dissimilar object categories and poses (Liu et al., 2019a; Zhu et al., 2017). Prior attempts to employ GANs for FSL augmentation typically restrict themselves to training-time augmentation (Hariharan & Girshick, 2017b; Schwartz et al., 2018; Hariharan & Girshick, 2017a). While generating data for seen classes is common, quality synthesis for unseen classes is challenging. To our best knowledge, Bai et al. (2025) is the only prior work explicitly using test-time generative augmentation for FSL (Liang et al., 2024), which relies on GAN-based image-to-image translation comprising two samples and focuses on animal faces instead of more-diverse

objects, limited in the broad dataset applicability (Liu et al., 2019a). A few recent work leverages diffusion-generated images for training data augmentation. However, the methods rely on fine-tuning using text prompts or additional target-class samples (Trabucco et al., 2024; He et al., 2023), thus not suitable for the challenging FSL test-time set-up.

We propose *1S-DAug* (One-Shot Data Augmentation), an operator that, given a single image at test time, synthesizes a set of diverse yet faithful variants. The operator combines three ingredients: (i) class-preserving shape perturbations to broaden pose and layout coverage; (ii) controlled noise injection to hide non-class-defining and distorted details; and (iii) denoising guided by attention-based conditioning on the original image so that content-defining cues are preserved while appearance and pose vary in a controlled manner. During few-shot classification, the generated variants are aggregated with the original representation. The method is model-agnostic and requires no retraining. As large pretrained models proliferate and model sizes continue to explode, fine-tuning or model-side ensemble can be burdensome or infeasible due to compute or **restricted parameter access** (Zheng et al., 2023). A test-time, data-side plugin that treats the predictor in model-agnostic ways is thus attractive. In experiments on four FSL benchmarks, our method yields consistent gains without modifying any model parameters.

Our contributions include:

- We introduce *1S-DAug*, a one-shot data augmentation method. Given a single image, it leverages attention-guided diffusion with controlled noise to generate faithful yet diverse variants suitable for inference on unseen classes. Though synthetic data augmentation with target-class supervision is not new, to the best of our knowledge, we are the **first** to focus on data augmentation given just one unlabelled image. Besides, 1S-DAug can fulfill the challenging FSL test-time augmentation requirement. As this direction is practically meaningful but **underexplored**, we analyse 1S-DAug’s integration with FSL.
- We offer clean, intuitive theoretical analyses for 1S-DAug, where we mainly separate the FSL generalization risk to the empirical risk and the Rademacher complexity term. Under idealized assumptions, 1S-DAug improves both the empirical risk via diversity and the Rademacher complexity term under shrunk data radius. Though the risk bound is standard, its adaptation to FSL concisely captures the design rationale.
- We implement 1S-DAug as a test-time plugin for trained FSL models, and we evaluate on benchmarks of four datasets, observing **consistent gains** (e.g., up to 20% relative improvement on 5-way-1-shot benchmarks) without any underlying parameter update to the

off-the-shelf models, which is practically meaningful.

## 2. Related Work

For **few-shot learning**, augmentation-based approaches expand training diversity via feature hallucination (Hariharan & Girshick, 2017a) or GAN-driven synthesis (Wang et al., 2018), but they are largely *training-time* and rely on supervision from base classes. In contrast, *test-time* augmentation for FSL is harder; it must generate high-quality, class-faithful variants for unseen classes without any retraining or labels. The only explicit work in this direction is FSL-Rectifier (Bai et al., 2025), which uses FUNIT (Liu et al., 2019a) to combine the shape of one image with the class-defining style of another. This serves as a proof of concept, mainly targeting animal-face datasets with limited broad applicability. For **diffusion models**, attention-based conditioning adapters now inject external signals (e.g., an input image) into cross-attention, enabling faithful, controllable generation (Mou et al., 2023). SDEdit (Meng et al., 2022) adds controlled noise and then denoises with conditioning. However, lower noise level yields minimal change, and the higher sacrifices faithfulness (e.g., change object type), thus not suitable as data augmentation that requires both diversity and faithfulness. There are a few recent works using the diffusion-based synthetic images for training augmentation outside of few-shot learning, but they rely on fine-tuning based on text prompts or additional test-class samples, and are thus limited for test-time augmentation (He et al., 2023; Benigmim et al., 2023; Trabucco et al., 2024). More related works are available in Appendix Section §F.

## 3. Diffusion Preliminaries

Let  $x_0 \in \mathcal{X}$  be an image and  $x_t$  its noised version at step  $t \in \{1, \dots, T\}$ . A variance schedule  $(\beta_t)_{t=1}^T$  defines  $\alpha_t = 1 - \beta_t$  and  $\bar{\alpha}_t = \prod_{\tau=1}^t \alpha_\tau$ . We use the variance-preserving (VP) forward process (Sohl-Dickstein et al., 2015; Ho et al., 2020; Nichol & Dhariwal, 2021; Meng et al., 2022)

$$q(x_t | x_0) = \mathcal{N}(\sqrt{\bar{\alpha}_t} x_0, (1 - \bar{\alpha}_t) \mathbf{I}), \quad (1)$$

so that sampling  $x_t$  can be written as  $x_t = \sqrt{\bar{\alpha}_t} x_0 + \sqrt{1 - \bar{\alpha}_t} \epsilon$  with  $\epsilon \sim \mathcal{N}(0, \mathbf{I})$ .

A user noise level  $\eta \in [0, 1]$  is mapped to a discrete start time  $t_0 \in \{1, \dots, T\}$  by matching cumulative noise:

$$t_0 = \arg \min_{t \in \{1, \dots, T\}} |(1 - \bar{\alpha}_t) - \eta^2|. \quad (2)$$

Let  $\hat{\epsilon}_\varphi$  be a learned noise predictor with parameters  $\varphi$ , and let  $c_t$  be the conditioning signal at time  $t$ . The VP reverse update is

$$x_{t-1} = \mu_\varphi(x_t, t, c_t) + \sigma_t \epsilon, \quad (3)$$

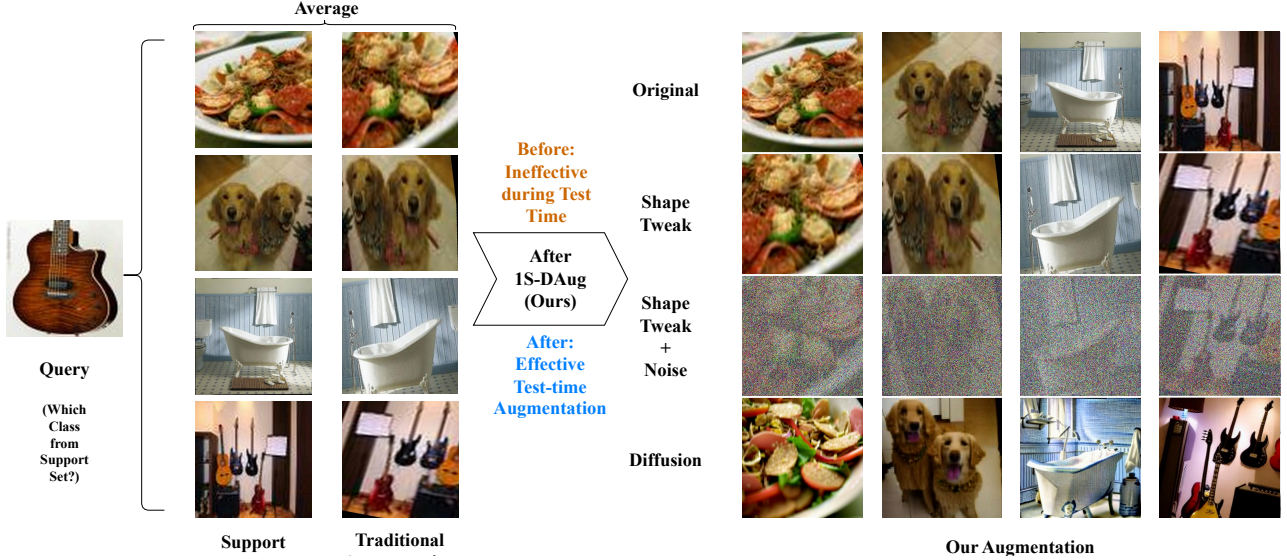


Figure 1. Pipeline of our one-shot, test-time augmentation. Given a query and supports, we apply a shape tweak and controlled noise, then perform attention-conditioned diffusion to synthesize class-faithful variants. Features from the original and the generated views are averaged before the few-shot head. For contrast, traditional test-time geometric transformations provide limited diversity.

with  $\epsilon \sim \mathcal{N}(0, \mathbf{I})$  and sampler noise level  $\sigma_t$  (we use  $\sigma_t=0$  in our experiments), where  $\mu_\varphi(x_t, t, c_t) = \alpha_t^{-1/2}(x_t - \frac{1-\alpha_t}{\sqrt{1-\bar{\alpha}_t}} \hat{\epsilon}_\varphi(x_t, t, c_t))$ . The same formulas apply in a latent space  $z_t$  via an encoder-decoder (Enc, Dec), with denoising output  $\tilde{x} = \text{Dec}(z_0)$  (Rombach et al., 2022a).

## 4. Method

**FSL Problem Setup.** We operate in standard inductive FSL classification, where a trained encoder  $\Phi_\theta : \mathcal{X} \rightarrow \mathbb{R}^d$  and a non-parametric classifier are evaluated on novel classes. Given a support set of labelled examples and an unlabelled query, the model must decide which support class the query belongs to. Typical FSL methods compute similarities between the query representation and the representations of support examples under a distance or similarity metric, and assign the query to the closest class prototype (Wang et al., 2020; Sung et al., 2018; Ye et al., 2020; Snell et al., 2017). In what follows we denote the encoder by  $\Phi_\theta$  but, when  $\theta$  is fixed, we often simply write  $\Phi$  for brevity. Our goal is to wrap any such trained FSL model with a training-free test-time augmentation operator that, given a single image, synthesises faithful yet diverse variants and aggregates their representations for prediction.

**1S-DAug.** We produce variants of a single image by (1) applying traditional geometric changes, (2) injecting a controlled amount of noise to determine edit magnitude, and (3) denoising via a diffusion process conditioned on the source image so that content-defining attributes are preserved while details and pose can vary. We write the resulting single-

image augmentation operator as

$$\mathcal{A}(x; v) = \text{Den}_\varphi\left(\text{Noi}_\eta(T_\psi(x)), \lambda_{\text{img}}\right) \in \mathcal{X}, \quad (4)$$

where  $v = (\psi, \eta, \lambda_{\text{img}})$  collects the geometric, noising, and conditioning hyperparameters;  $T_\psi$  is a sampled geometric transform;  $\text{Noi}_\eta$  (add noise) applies the forward diffusion process up to a start time  $t_0$  determined by the noise level  $\eta$  (e.g. via (2)); and  $\text{Den}_\varphi$  (denoise), parametrized by fixed diffusion parameters  $\varphi$ , runs the reverse process from  $t_0$  to 0 with image-conditioned attention. We next detail each stage of this operator.

**Stage 1: Shape Tweak.** Changes in pose/layout increase coverage of plausible views without altering class identity. Let  $\psi$  be shape-tweak parameters and

$$x_{\text{geom}} = T_\psi(x),$$

where  $T_\psi$  is drawn from a family of traditional image transformations, composed as rotations, anisotropic stretches, translations, perspective jitters, and horizontal flips.

**Stage 2: Controlled Noising.** The noise level sets the change magnitude during the diffusion denoising pipeline. Lower noise emphasises faithfulness; higher noise hides geometric distortion better and yields more diversity. We use the variance-preserving (VP) forward kernel (Sohl-Dickstein et al., 2015; Ho et al., 2020; Nichol & Dhariwal, 2021; Meng et al., 2022). Let  $t \in \{1, \dots, T\}$  index discrete diffusion steps, let  $\beta_t \in (0, 1)$  be a variance schedule, and define  $\alpha_t := 1 - \beta_t$  and  $\bar{\alpha}_t := \prod_{\tau=1}^t \alpha_\tau$ . Given a user noise

level  $\eta \in [0, 1]$ , we choose a start time  $t_0 = t(\eta)$  (e.g., by matching cumulative noise as in (2)), and sample

$$x_{t_0} \sim q(x_{t_0} | x_{\text{geom}}) = \mathcal{N}\left(\sqrt{\bar{\alpha}_{t_0}} x_{\text{geom}}, (1 - \bar{\alpha}_{t_0}) \mathbf{I}\right), \quad (5)$$

where  $x_{\text{geom}}$  is the geometrically perturbed input (Stage 1),  $\mathbf{I}$  is the identity covariance, and  $\mathcal{N}$  denotes a Gaussian distribution.

**Stage 3: Image-Conditioned Diffusion Denoising.** Let  $z_t$  be the latent at time  $t$ , and let  $f_{\text{img}}(x) \in \mathbb{R}^{L \times d_k}$  and  $f_{\text{txt}}(p) \in \mathbb{R}^{M \times d_k}$  be fixed-encoder outputs for the condition image  $x$  and optional text prompt  $p$ . For a U-Net (Ronneberger et al., 2015) block at time  $t$ , with queries  $Q_t = W_Q z_t \in \mathbb{R}^{N_q \times d_k}$  (here  $W_Q$  denotes the query weights and biases and  $N_q$  is the number of query tokens) and keys/values  $K_t, V_t \in \mathbb{R}^{(M+L) \times d_k}$ , the cross-attention (Vaswani et al., 2017) is

$$A_t(Q_t, K_t, V_t) = \text{softmax}\left(\frac{Q_t K_t^\top}{\sqrt{d_k}}\right) V_t, \quad (6)$$

and we concatenate text/image tokens with a scalar weight  $\lambda_{\text{img}} \geq 0$ :

$$K_t = [K_t^{\text{txt}}, \lambda_{\text{img}} K_t^{\text{img}}], \quad V_t = [V_t^{\text{txt}}, \lambda_{\text{img}} V_t^{\text{img}}], \quad (7)$$

with  $K_t^{\text{txt}}, V_t^{\text{txt}} = W_{\text{txt},t} f_{\text{txt}}(p)$  and  $K_t^{\text{img}}, V_t^{\text{img}} = W_{\text{img},t} f_{\text{img}}(x)$ . We set the conditioning variable for the reverse update to  $c_t := A_t(Q_t, K_t, V_t)$ . The VP reverse step (3) then reads

$$z_{t-1} = \mu_\varphi(z_t, t, c_t) + \sigma_t \epsilon, \quad \epsilon \sim \mathcal{N}(0, \mathbf{I}), \quad (8)$$

and rolling out  $t_0 \rightarrow 0$  produces  $\tilde{x} = \text{Dec}(z_0)$ .

**FSL Feature Aggregation.** Averaging features over faithful but non-identical views draws representations toward class-typical regions and improves robustness for non-parametric few-shot classifiers (Snell et al., 2017; Chen et al., 2019; Ye et al., 2020; Bai et al., 2025). For each image  $x$  we generate  $K_a^{\text{sup}} + 1$  support views  $\tilde{x}^{(k)} = \mathcal{A}(x; v^{(k)})$  with  $\tilde{x}^{(0)} \equiv x$ , where each  $v^{(k)}$  denotes a fresh sample of augmentation hyperparameters, and form an aggregated support embedding

$$\bar{z}_{\text{sup}}(x) = \sum_{k=0}^{K_a^{\text{sup}}} \alpha_k^{\text{sup}} \Phi(\tilde{x}^{(k)}), \quad \alpha_k^{\text{sup}} \geq 0, \quad \sum_{k=0}^{K_a^{\text{sup}}} \alpha_k^{\text{sup}} = 1. \quad (9)$$

Given a support set  $S = \{(s_i, y_i)\}_{i=1}^{NK}$  with  $N$  classes and  $K$  shots per class, class prototypes are  $p_c = \frac{1}{K} \sum_{i: y_i=c} \bar{z}_{\text{sup}}(s_i)$ . For each query  $q$  we generate  $K_a^{\text{qry}} + 1$  query views  $\tilde{q}^{(k)} = \mathcal{A}(q; v^{(k)})$ , encode them as  $z^{(k)}(q) = \Phi(\tilde{q}^{(k)})$ , and compute per-view logits  $\ell_c^{(k)}(q) =$

$\kappa(z^{(k)}(q), p_c)$  for a chosen similarity  $\kappa$  (Euclidean or cosine). We then perform query-side logit averaging for FSL prediction:

$$\begin{aligned} \tilde{\ell}_c(q) &:= \sum_{k=0}^{K_a^{\text{qry}}} \alpha_k^{\text{qry}} \ell_c^{(k)}(q), \quad \alpha_k^{\text{qry}} \geq 0, \quad \sum_{k=0}^{K_a^{\text{qry}}} \alpha_k^{\text{qry}} = 1, \\ \hat{y}(q) &= \arg \max_{c \in \{1, \dots, N\}} \tilde{\ell}_c(q). \end{aligned} \quad (10)$$

## 5. Theoretical Analyses

We analyse 1S-DAug in the standard episodic few-shot setting with a single trainable encoder and a fixed Euclidean nearest-prototype classifier. We show that (i) a simple risk decomposition emphasises accuracy and diversity, and (ii) a tightened margin-based generalisation bound after augmentation, via both empirical margin and feature-radius reduction. Lastly, based on the bound, we compare training and test-time augmentation in Appendix B.6. Note that we focus on the overall theoretical logic instead of the details, which is simplifying but self-contained and sufficient to illustrate the design’s logical coherence.

### 5.1. Episodic Euclidean Model and Test-Time Augmentation

We consider the encoder-plus-Euclidean-prototype classifier of Section 4. In an  $N$ -way  $K$ -shot episode, class prototypes  $p_c$  are formed by averaging support embeddings, and a query  $q$  is assigned to the nearest prototype in squared Euclidean distance  $\|\Phi_\theta(q) - p_c\|_2^2$ . For the theory we reduce episodes to binary query-prototype pairs  $x = (q, p)$  with label  $y \in \{-1, 1\}$ , write

$$\Omega_\theta(x) := \Phi_\theta(q) - p \quad \text{and} \quad g_\theta(x) := -\|\Omega_\theta(x)\|_2^2,$$

and assume a uniform radius bound  $\|\Omega_\theta(x)\|_2 \leq r_0$ . Under test-time augmentation, multiple query views are combined by logit averaging; for squared Euclidean scores this is equivalent to using an averaged query embedding and hence an aggregated difference feature  $\bar{\Omega}_\theta(x)$ . Full episodic details and the logit-feature equivalence are deferred to Appendix B.1 and B.3.

### 5.2. Risk Decomposition into Accuracy and Diversity

We first quantify the ensemble effect at the pairwise level. For any real-valued predictor  $g$  on pairs  $x = (q, p)$  we use the scaled squared-loss risk

$$\mathcal{R}(g) := \frac{1}{4} \mathbb{E}_{(x,y) \sim D} [(g(x) - y)^2], \quad (11)$$

which coincides with 0-1 pairwise error when  $g(x) \in \{-1, 1\}$ . In particular, if  $g_\theta$  is a sign-valued score, the pairwise misclassification risk  $R_{\text{cls}}(\theta) := \mathbb{P}_{(x,y) \sim D}(y g_\theta(x) \leq$

0) satisfies  $R_{\text{cls}}(\theta) = \mathcal{R}(g_\theta)$ . Let  $f(x)$  and  $f_A(x)$  be the sign predictors associated with the base and an augmented view, and define the (two-view) ensemble  $\tilde{f}(x) := \frac{1}{2}(f(x) + f_A(x)) \in \{-1, 0, 1\}$ . A direct calculation (Appendix A) yields:

**Proposition 5.1** (Pairwise Risk Decomposition). *With  $\mathcal{R}(\cdot)$  as in (11),*

$$\begin{aligned} & \mathcal{R}(\tilde{f}) - \mathcal{R}(f) \\ &= \underbrace{\frac{1}{4}(\mathbb{E}[f(x)y] - \mathbb{E}[f_A(x)y])}_{\text{accuracy gap}} + \underbrace{\frac{1}{8}(\mathbb{E}[f(x)f_A(x)] - 1)}_{\text{diversity term}}. \end{aligned} \quad (12)$$

Thus improvements come from (i) maintaining or improving single-view accuracy, and (ii) making the augmented predictions sufficiently diverse on hard examples. This matches the empirical behaviour of 1S-DAug, which is designed to generate plausible but different-shape query views.

### 5.3. Encoder Generalisation and Radius Reduction

In the pairwise reduction of §Section 5.1, each example is a query-prototype pair  $x = (q, p)$  with label  $y \in \{-1, +1\}$ , difference feature  $\Omega_\theta(x) := \Phi_\theta(q) - p$ , and squared-Euclidean score  $g_\theta(x) := -\|\Omega_\theta(x)\|_2^2$ . We write the pairwise 0-1 risk as  $R_{\text{cls}}(\theta) := \mathbb{P}_{(x,y) \sim D}(y g_\theta(x) \leq 0)$ , and assume the uniform pre-augmentation radius bound  $\|\Omega_\theta(x)\|_2 \leq r_0$ . Under test-time augmentation, query logit averaging is equivalent (up to a class-independent constant) to nearest-prototype classification using the averaged query embedding (Section 5.1, formalized in Appendix B.3); hence we may analyze the aggregated feature  $\bar{\Omega}_\theta(x)$  and aggregated score  $\bar{g}_\theta(x) := -\|\bar{\Omega}_\theta(x)\|_2^2$ .

**Margin Generalisation Bound.** Let  $u_\theta(x) := y g_\theta(x)$  denote the signed margin and let  $\tau_\rho$  be the standard  $\rho$ -margin surrogate (Appendix B.2). For a sample  $S = \{(x_i, y_i)\}_{i=1}^m$ , define the empirical margin risk  $\hat{R}_{S,\rho}(\theta) := \frac{1}{m} \sum_{i=1}^m \tau_\rho(u_\theta(x_i))$  and the empirical Rademacher complexity  $\hat{\mathfrak{R}}_S(\mathcal{G})$  of the score class  $\mathcal{G} := \{g_\theta : \theta \in \Theta\}$ . The following is a standard contraction-based margin bound (proof in Appendix B.2).

**Theorem 5.2** (Encoder margin bound). *For any  $\rho > 0$  and  $\delta \in (0, 1)$ , with probability at least  $1 - \delta$  over  $S \sim D^m$ , every  $\theta$  satisfies*

$$R_{\text{cls}}(\theta) \leq \hat{R}_{S,\rho}(\theta) + \frac{2}{\rho} \hat{\mathfrak{R}}_S(\mathcal{G}) + \sqrt{\frac{\log(1/\delta)}{2m}}. \quad (13)$$

To make the complexity term explicit for Euclidean scores, we control  $\hat{\mathfrak{R}}_S(\mathcal{G})$  via the encoder Lipschitz constant and the feature radius (proof sketch in Appendix B.2).

**Lemma 5.3** (Rademacher control via radius). *Assume  $\Phi_\theta$  is realised by a feedforward network with 1-Lipschitz nonlinearities and layer spectral norms whose product is bounded by  $L_{\text{enc}}$ , and assume a uniform radius bound  $\|\Omega_\theta(x)\|_2 \leq r$  for all  $x$  and  $\theta$ . Then there exists an architecture-dependent constant  $C_{\text{enc}} > 0$  such that  $\hat{\mathfrak{R}}_S(\mathcal{G}) \leq C_{\text{enc}} L_{\text{enc}} \frac{r}{\sqrt{m}}$ .*

Combining Theorem 5.2 and Lemma 5.3 yields a bound in which the complexity term scales linearly with the *effective feature radius*. This is the mechanism by which aggregation can tighten generalisation.

**Why Test-time Aggregation Works.** Let  $\hat{S}$  denote the same labeled pairs as  $S$  but evaluated with aggregated difference features  $\bar{\Omega}_\theta(x_i)$  and aggregated score  $\bar{g}_\theta$ . Applying Theorem 5.2 to  $\bar{g}_\theta$  yields the same bound with  $\hat{R}_{S,\rho}(\theta)$  replaced by  $\hat{R}_{\hat{S},\rho}(\theta)$  and the radius parameter  $r$  replaced by an aggregated radius  $\hat{r}$  such that  $\|\bar{\Omega}_\theta(x)\|_2 \leq \hat{r}$ . Since Lemma 5.3 is linear in  $r$ , any contraction  $\hat{r} < r_0$  directly contracts the complexity term. A simple stability statement relates the empirical margin risks before and after aggregation (proof in Appendix B.4).

**Proposition 5.4** (Probabilistic radius reduction with  $M$  augmentations). *Let  $\{\Omega_i^{(k)}\}_{i=1,k=0}^{m,M}$  be i.i.d. from a continuous distribution and  $\hat{\Omega}_i := \frac{1}{M+1} \sum_{k=0}^M \Omega_i^{(k)}$ . Writing  $R_{\text{orig}}^{\max} := \max_i \|\Omega_i^{(0)}\|_2$  and  $\hat{R}^{\max} := \max_i \|\hat{\Omega}_i\|_2$ , we have  $\mathbb{P}(\hat{R}^{\max} < R_{\text{orig}}^{\max}) \geq \frac{1}{M+1}$ .*

Proof is in Appendix B.5. Taken together, Lemma 5.3 and Proposition 5.4 illustrate that the multi-view aggregation can tighten the complexity term through radius contraction. Additionally, the potentially reduced risk empowered by both accuracy and diversity as specified in Section §5.2 also indicates lower empirical risk compared to before the augmentation. Therefore, the overall generalization bound in 5.2 tends to tighten.

**Training-time Versus Test-time Augmentation.** Training-time augmentation on base classes primarily tightens a bound on the *base* risk by increasing sample size, but any transfer to novel classes typically incurs an additional distribution-shift discrepancy term. In contrast, 1S-DAug targets the novel classes directly. More discussions are available in Appendix B.6.

## 6. Experiments

**Datasets and Pre-processing.** We follow the standard 5-way-1/5-shot episodic evaluation on miniImagenet and tieredImageNet (Russakovsky et al., 2015); additional experiments are conducted on CUB (fine-grained birds) (Wah et al., 2011) and an animal-face dataset used previously for test-time augmentation studies (Animals) (Liu et al., 2019a;

Table 1. Inductive 5-way-1-shot and 5-way-5-shot accuracy (%) on miniImagenet and tieredImageNet with Res12 backbones. Dashes denote unavailable or less important results not reported. The best results of ours and other FSL methods are both highlighted in bold. Our method transforms the weaker models to become stronger than most of the other Res12 baselines; we can likely achieve even better performance using stronger base models.

Method (Res12)	5-Way-1-Shot (%)		5-Way-5-Shot (%)	
	miniImagenet	tieredImageNet	miniImagenet	tieredImageNet
DeepEMD (Zhang et al., 2020)	65.91 $\pm$ 0.82	71.16 $\pm$ 0.87	82.41 $\pm$ 0.56	<b>86.03</b> $\pm$ 0.58
Meta-MaxUp (Ni et al., 2020)	62.81 $\pm$ 0.34	-	79.38 $\pm$ 0.24	-
Meta-Baseline (Chen et al., 2021)	63.17 $\pm$ 0.23	68.62 $\pm$ 0.27	79.26 $\pm$ 0.17	83.74 $\pm$ 0.18
MetaOptNet (Lee et al., 2019)	62.64 $\pm$ 0.61	65.99 $\pm$ 0.72	78.63 $\pm$ 0.46	81.56 $\pm$ 0.53
SLA-AG (Lee et al., 2020)	62.93 $\pm$ 0.63	-	79.63 $\pm$ 0.47	-
ProtoNet + TRAML (Li et al., 2020)	60.31 $\pm$ 0.48	-	77.94 $\pm$ 0.57	-
ConstellationNet (Xu et al., 2021)	64.89 $\pm$ 0.23	-	79.95 $\pm$ 0.17	-
Classifier-Baseline (Chen et al., 2021)	58.91 $\pm$ 0.23	68.07 $\pm$ 0.26	77.76 $\pm$ 0.17	83.74 $\pm$ 0.18
DFR (Cheng et al., 2023)	<b>67.74</b> $\pm$ 0.86	<b>71.31</b> $\pm$ 0.93	<b>82.49</b> $\pm$ 0.57	85.12 $\pm$ 0.64
ProtoNet-Res12 (Snell et al., 2017)	62.39 $\pm$ 0.21	68.23 $\pm$ 0.23	80.53 $\pm$ 0.14	84.03 $\pm$ 0.16
ProtoNet-Res12 (re-impl.)	60.01 $\pm$ 0.65	65.28 $\pm$ 0.32	75.34 $\pm$ 0.49	81.13 $\pm$ 0.29
ProtoNet-Res12+1S-DAug-1 (Ours)	62.90 $\pm$ 0.66 (+2.89% $\uparrow$ )	69.06 $\pm$ 0.32 (+3.78% $\uparrow$ )	78.89 $\pm$ 0.48 (+3.55% $\uparrow$ )	83.86 $\pm$ 0.27 (+2.73% $\uparrow$ )
ProtoNet-Res12+1S-DAug-2 (Ours)	64.61 $\pm$ 0.66 (+4.60% $\uparrow$ )	70.32 $\pm$ 0.32 (+5.04% $\uparrow$ )	-	-
ProtoNet-Res12+1S-DAug-3 (Ours)	64.94 $\pm$ 0.66 (+4.93% $\uparrow$ )	-	-	-
FEAT-Res12 (Ye et al., 2020)	66.78 $\pm$ 0.20	70.80 $\pm$ 0.23	82.05 $\pm$ 0.14	84.79 $\pm$ 0.16
FEAT-Res12 (re-impl.)	63.31 $\pm$ 0.65	68.28 $\pm$ 0.28	77.90 $\pm$ 0.48	82.21 $\pm$ 0.28
FEAT-Res12+1S-DAug-1 (Ours)	67.08 $\pm$ 0.65 (+3.77% $\uparrow$ )	71.85 $\pm$ 0.28 (+3.57% $\uparrow$ )	81.96 $\pm$ 0.44 (+4.06% $\uparrow$ )	84.82 $\pm$ 0.26 (+2.61% $\uparrow$ )
FEAT-Res12+1S-DAug-2 (Ours)	69.04 $\pm$ 0.65 (+5.73% $\uparrow$ )	<b>73.18</b> $\pm$ 0.27 (+4.90% $\uparrow$ )	82.62 $\pm$ 0.45 (+4.72% $\uparrow$ )	<b>85.55</b> $\pm$ 0.25 (+3.34% $\uparrow$ )
FEAT-Res12+1S-DAug-3 (Ours)	<b>69.25</b> $\pm$ 0.65 (+5.94% $\uparrow$ )	-	<b>83.38</b> $\pm$ 0.41 (+5.48% $\uparrow$ )	-

Table 2. Inductive 5-way-1-shot accuracy (%) on Animals with Res12 backbones and CUB with ConvNet backbones.

Method (Res12/ConvNet)	Animals	CUB
ProtoNet	73.20 $\pm$ 0.63	46.38 $\pm$ 0.22
ProtoNet+1S-DAug-2 (Ours)	75.20 $\pm$ 0.65 (+2.00% $\uparrow$ )	55.50 $\pm$ 0.24 (+9.12% $\uparrow$ )
FEAT	79.37 $\pm$ 0.59	51.10 $\pm$ 0.24
FEAT+1S-DAug-2 (Ours)	<b>80.66</b> $\pm$ 0.62 (+1.23% $\uparrow$ )	<b>61.55</b> $\pm$ 0.25 (+10.45% $\uparrow$ )

Table 3. 5-way-1-shot accuracy (%) on miniImagenet/CUB with ViTSmall/SwinTiny backbones.

Dataset	Method	ViTSmall	SwinTiny
MiniImagenet	ProtoNet (Snell et al., 2017)	71.86	67.32
	ProtoNet+1S-DAug-1 (Ours)	80.42 (+8.56% $\uparrow$ )	75.12 (+7.80% $\uparrow$ )
	ProtoNet+1S-DAug-2 (Ours)	82.76 (+10.90% $\uparrow$ )	77.82 (+10.50% $\uparrow$ )
	ProtoNet+1S-DAug-3 (Ours)	83.66 (+11.80% $\uparrow$ )	78.92 (+11.60% $\uparrow$ )
CUB	ProtoNet (Snell et al., 2017)	71.90	69.78
	ProtoNet+1S-DAug-1 (Ours)	75.72 (+3.82% $\uparrow$ )	71.76 (+1.98% $\uparrow$ )

Bai et al., 2025). We adhere to the conventional train/val/test splits for each benchmark. Besides, we set the aggregation weight of the original image as 0.5, and additional images as 0.5 altogether, so as to emphasize the original images. For diffusion noise addition, we set the noise level to 0.7. Details are available in Appendix E.

**Evaluation Protocol.** We evaluate three standard backbones used in FSL: a shallow 4-layer convolutional neural network (ConvNet), a 12-layer residual network (Res12) (He et al., 2016), a small vision transformer backbone (ViTSmall) (Dosovitskiy et al., 2021) and a tiny swin transformer backbone (SwinTiny) (Liu et al., 2021). Note that the encoders ViTSmall and SwinTiny are pretrained on the

ImageNet-1k (Russakovsky et al., 2015) dataset, while the Res12 and ConvNet encoders are trained on the train-split of each FSL dataset. Classification is performed with a non-parametric Euclidean-distance/cosine-similarity prototype classifier in the episodic setting. These choices match common FSL practice, including ProtoNet and FEAT-style set-to-set variants that operate on support/query embeddings, ensuring comparability with prior work and our reproduced baselines (Snell et al., 2017; Ye et al., 2020). We evaluate off-the-shelf trained ProtoNet and FEAT models. We adopt Euclidean-distance-based classifier for miniImagenet and tieredImageNet, and cosine-similarity-based classifier for Animals and CUB. Our reproduced baselines closely match prior reports evaluation set-up (e.g., DeepEMD (Zhang et al., 2020), Meta-Baseline (Chen et al., 2021), MetaOptNet (Lee et al., 2019) on 5-way-1/5-shot inductive benchmarks, all with the Res12 backbone. Among the baselines, SLA-AG (Lee et al., 2020) involves self-supervised label augmentation, and Meta-MaxUp (Ni et al., 2020) involves training data augmentation, both being ensemble-based methods.). We sample 15,000 5-way-1/5-shot queries and report mean accuracy with 95% confidence intervals across episodes. This follows the standard protocol used in related FSL work (Ye et al., 2020; Snell et al., 2017).

**Main Results.** Table 1/2/3 summarizes 5-way-1-shot and 5-way-5-shot results with Res12/ConvNet/ViTSmall/SwinTiny backbones, and our method with 1/2/3 additional augmentations are denoted as 1S-DAug-1/2/3 respectively. Note that we directly adopt

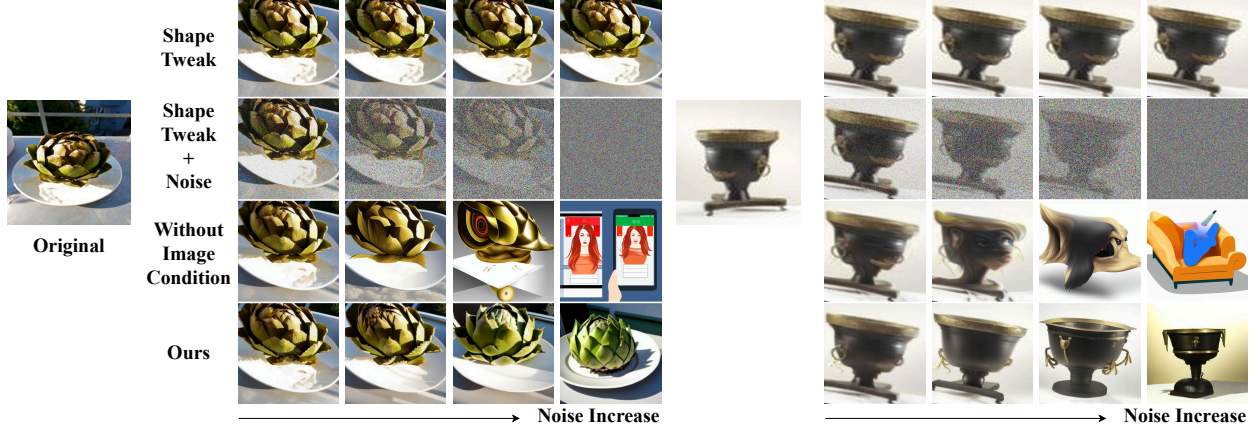


Figure 2. Effect of noise and conditioning. Qualitative ablation on a single input across increasing noise levels. Shape-only edits yield limited diversity; adding noise increases diversity but may reduce fidelity without conditioning. Attention-conditioned diffusion preserves class-defining content while enabling controlled pose/appearance changes; excessive noise without the image condition degrades faithfulness.

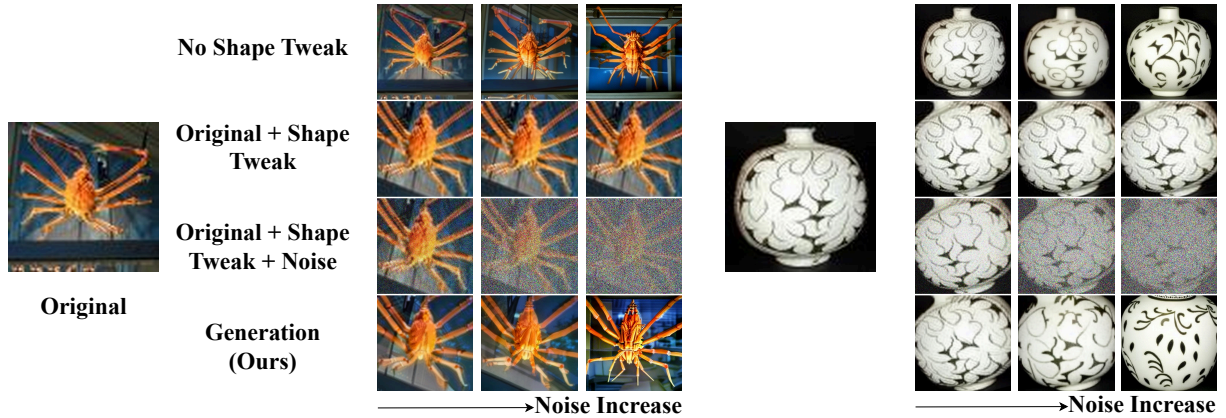


Figure 3. Effect of noise and shape tweak. Comparison across three settings: no shape tweak, shape tweak only, and shape + noise + attention-conditioned diffusion (ours). Increasing noise and including shape tweak expand diversity, and our full setting provides the best for both diversity and faithfulness.

5-way-1-shot FSL models for the 5-way-5-shot evaluation, and Table 2 contains 5-way-1-shot results on CUB and Animals. As reported, test-time 1S-DAug consistently improves over the corresponding non-augmented baselines and over prior strong Res12 methods reported under the same backbone (e.g., on miniImagenet, FEAT improves from 63.31% to 69.25%, a maximum absolute gain of +5.94 percentage points, which achieves the highest among all the reported FSL works with Res12 backbones). Note that our method performs significantly better on the Animals dataset compared to the prior work that uses GAN reconstruction, which only achieves 57.90% on the 5-way-1-shot setup with one augmentation (Bai et al., 2025). The limitation GAN generation quality has been discussed in (Bai et al., 2025; Liu et al., 2019a), and the related failure case visualization is available in Appendix Figure 4. All our gains persist across 4 datasets (e.g., miniImagenet improves by at least +2.89%, tieredImageNet

by +3.88%, CUB by +9.12%, and Animals by +1.23% on the 5-way-1-shot benchmarks), implying a high probability for: (i) the image-conditioned diffusion step preserves class-defining content sufficiently, and (ii) the shape tweak with noising creates diversity without compromising faithfulness. Additionally, ViTSmall/SwinTiny backbones are pretrained on ImageNet-1k (Russakovsky et al., 2015), and we still achieve consistent non-trivial improvement over these more knowledgeable backbones.

**How Much and Where to Augment.** We ablate support-only, query-only, and joint support+query augmentation under ProtoNet (Res12) on miniImagenet. See our ablation table (Table 5) for the full grid. Accuracy improves monotonically as we add a number of augmented copies to *both* support and queries (e.g., from 60.01% with no augmentation to 64.94% with +3/3, yielding a +4.93 absolute gain). Adding only support copies while leaving

Table 4. Inductive 5-way-1-shot accuracy (mean  $\pm$  95% CI) as a function of the number of augmented copies for supports (rows) and queries (columns).

		Query			
		+0	+1	+2	+3
Support	+0	60.01 $\pm$ 0.65	60.24 $\pm$ 0.69	60.09 $\pm$ 0.70	60.31 $\pm$ 0.70
	+1	60.20 $\pm$ 0.66	62.90 $\pm$ 0.66	63.05 $\pm$ 0.67	63.16 $\pm$ 0.67
	+2	61.80 $\pm$ 0.64	64.53 $\pm$ 0.66	64.61 $\pm$ 0.66	64.87 $\pm$ 0.66
	+3	61.82 $\pm$ 0.64	64.55 $\pm$ 0.65	64.72 $\pm$ 0.66	64.94 $\pm$ 0.66

Table 5. Ablation of aggregation weight adjustment, shape tweak, noise level, and diffusion conditioning. ‘Traditional’ uses standard geometric edits; ‘Real’ substitutes actual additional images of the same object type. Our full setting (shape + controlled noise + attention-conditioned diffusion) outperforms classical test-time augmentation and approaches the oracle (true image) upper bound.

Same Noise Level	Shape Tweak	Generation Techniques	Additional Adjustment	5-Way-1-Shot Accuracy
✓(0.70)	✓	✓	✓ (0.3 original image weight)	66.79 $\pm$ 0.63
✓(0.70)	✓	✓	✓ (remove image conditioning)	53.94 $\pm$ 0.62
✗(0.20)	✓	✓	✗	63.45 $\pm$ 0.64
✓(0.70)	✓	✓	✗	67.08 $\pm$ 0.62
✗(1.00)	-	✓	✗	67.01 $\pm$ 0.68
✓(0.70)	✗	✓	✗	66.12 $\pm$ 0.66
-	✓ (Real/Oracle)	✗	✗	77.99 $\pm$ 0.62
-	✓ (Traditional)	✗	✗	57.89 $\pm$ 0.67

queries un-augmented can underperform due to distribution mismatch between prototype construction and query embeddings (e.g., with +3/0 accuracy is 61.82%, well below the 64.55% achieved when queries are matched with +3/1). This suggests that matched augmentation on both sides yields the largest benefit.

**Qualitative Ablation Studies.** Figure 2 illustrates the effect of removing image conditioning/shape tweaks, and changing the noise level. With small noise, changes are minimal; with large noise and no image conditioning, generations may drift toward off-class content; removing shape tweaks reduces diversity and visible pose/layout variations. More visualizations are provided in Appendix J.

**Quantitative Ablation Studies.** We further dissect the contribution of each component, including aggregation weight adjustment, image conditioning, noise magnitude, shape tweaking and diffusion generation using FEAT with a Res12 backbone on miniImagenet, in a controlled 5-way-1-shot setting with one augmented query and one augmented support per episode (Table 4). We first notice that reducing the emphasis on original samples via less aggregation weight would downgrade model accuracy slightly. This is expected, since the original samples are authentic images with the best quality. Besides, removing the image conditioning downgrades the performance severely, which mirrors our qualitative studies in Figure 2. When a small noise level ( $\eta=0.20$ ) is applied with shape tweaking and conditioning, diversity gain is limited, and distortion caused by shape tweaking may also stay and backfire, yielding

63% accuracy. Increasing the noise strength to a moderate level ( $\eta=0.70$ ) improves coverage while preserving class faithfulness, pushing performance to 67.1%, the best among diffusion-based rows. Pushing noise to the extreme ( $\eta=1.0$ ) still delivers reasonable performance (67.0%) when conditioning is enabled. Such a performance is enabled by the greater diversity between the generation output and the original input, but the originality faithfulness is jeopardized, especially when confronted with rare object types. Therefore, generation from full noise should be discouraged. Besides, ablating shape tweaks reduces accuracy to 66.1%, confirming that geometric variation helps cover different pose/layout. Substituting true extra images of the same class (“Real/Oracle”) provides an upper bound of 78.0%, showing the headroom available with more independent samples. Meanwhile, traditional geometric test-time edits (rotations, affine warps, color jitter) only reach 57.89%, supporting the observation that such transforms add little new information and may distort original images.

## 7. Limitations and Future Work

Our approach has two main implementation limitations. *First*, the augmentation introduces inference overhead (See Appendix C). Reducing computational cost (e.g., via lighter generative backbones or faster denoising schedules) is useful, but the overhead can automatically attenuate as computation infrastructure develops. *Second*, we use the Stable-Diffusion-v1.5 generator (Rombach et al., 2022b), where we partially go beyond the FSL training data split. However, the FSL training splits are generally not enough to train a good-performing stable diffusion model, while the standard pretrained models are already available. Therefore, choosing the pretrained model is natural in both the real-world and research set-up. Also, we freeze all pretrained models and do not fine-tune on the test set. Importantly, our main contribution is not the specific implementation, but the algorithm design that scales with computation development.

## 8. Conclusions

To conclude, we presented *1S-DAug*, a one-shot test-time generative augmentation operator that synthesizes diverse yet faithful variants from a single image. By combining geometric perturbations with controlled noising and image-conditioned denoising, the method maintains class-defining content while enhancing diversity. A plugin into frozen FSL models, 1S-DAug delivers consistent non-trivial accuracy gains across different datasets, without even specific parameter access. This model-agnostic, data-side design makes the approach practically meaningful for deployments with large, fixed or restricted model. Overall, we believe 1S-DAug offers a high-potential building block for robustness under real-world low-label scenarios.

## 9. Impact Statement

1S-DAug is a single-image augmentation method that can improve few-shot generalization by producing diverse, label-preserving variants without requiring predictors' fine-tuning or specific model parameters. Assuming high quality of the pretrained image generator, such augmentation can improve accuracy and robustness in data-scarce settings and under distribution shift, which is particularly relevant in high-stakes perception pipelines (e.g., autonomous driving and medical imaging) where generalization failures can have serious consequences. By generating task-specific variants directly from a readily available pretrained model, the approach reduces both prediction error and the computational and data-collection costs typically associated with retraining, fine-tuning, and restricted model parameter access (e.g., API-only or proprietary deployments). Moreover, the method is likely useful beyond FSL, empowering applications such as training data augmentation and controllable image editing.

In safety-critical deployments, any gains from augmentation should be verified with rigorous testing and human oversight consistent with regulatory standards.

## References

Bai, Y., Tan, Y. K., Chen, S., Shu, Y., and Chen, T. Fsl-rectifier: Rectify outliers in few-shot learning via test-time augmentation. In *Proceedings of the AAAI Conference on Artificial Intelligence*, volume 39, pp. 15462–15471, 2025.

Bartlett, P. L. and Mendelson, S. Rademacher and gaussian complexities: Risk bounds and structural results. *Journal of Machine Learning Research*, 3:463–482, 2002.

Benigmim, Y., Roy, S., Essid, S., Kalogeiton, V., and Lathuilière, S. One-shot unsupervised domain adaptation with personalized diffusion models. In *Proceedings of the IEEE/CVF Conference on Computer Vision and Pattern Recognition Workshops (CVPRW)*, pp. 698–708, June 2023. URL [https://openaccess.thecvf.com/content/CVPR2023W/GCV/papers/ Benigmim\\_One-Shot\\_Unsupervised\\_Domain\\_Adaptation\\_With\\_Personalized\\_Diffusion\\_Models\\_CVPRW\\_2023\\_paper.pdf](https://openaccess.thecvf.com/content/CVPR2023W/GCV/papers/Benigmim_One-Shot_Unsupervised_Domain_Adaptation_With_Personalized_Diffusion_Models_CVPRW_2023_paper.pdf).

Chen, W.-Y., Liu, Y.-C., Kira, Z., Wang, Y.-C. F., and Huang, J.-B. A closer look at few-shot classification. *arXiv preprint arXiv:1904.04232*, 2019.

Chen, Y., Liu, Z., Xu, H., Darrell, T., and Wang, X. Meta-baseline: Exploring simple meta-learning for few-shot learning. In *Proceedings of the IEEE/CVF International Conference on Computer Vision (ICCV)*, 2021.

Cheng, H., Wang, Y., Li, H., Kot, A. C., and Wen, B. Disentangled feature representation for few-shot image classification. *IEEE transactions on neural networks and learning systems*, 35(8):10422–10435, 2023.

Dosovitskiy, A., Beyer, L., Kolesnikov, A., Weissenborn, D., Zhai, X., Unterthiner, T., Dehghani, M., Minderer, M., Heigold, G., Gelly, S., Uszkoreit, J., and Houlsby, N. An image is worth 16x16 words: Transformers for image recognition at scale. In *International Conference on Learning Representations (ICLR)*, 2021.

Dvornik, N., Schmid, C., and Mairal, J. Diversity with cooperation: Ensemble methods for few-shot classification. In *Proceedings of the IEEE/CVF international conference on computer vision*, pp. 3723–3731, 2019.

Finn, C., Abbeel, P., and Levine, S. Model-agnostic meta-learning for fast adaptation of deep networks. In *ICML*, 2017.

Hariharan, B. and Girshick, R. Low-shot visual recognition by shrinking and hallucinating features. In *Proceedings of the IEEE international conference on computer vision*, pp. 3018–3027, 2017a.

Hariharan, B. and Girshick, R. Low-shot visual recognition by shrinking and hallucinating features. In *CVPR*, 2017b.

He, K., Zhang, X., Ren, S., and Sun, J. Deep residual learning for image recognition. In *Proceedings of the IEEE conference on computer vision and pattern recognition*, pp. 770–778, 2016.

He, R., Sun, S., Yu, X., Xue, C., Zhang, W., Torr, P., Bai, S., and Qi, X. Is synthetic data from generative models ready for image recognition? In *Proceedings of the International Conference on Learning Representations (ICLR)*, 2023. URL <https://openreview.net/forum?id=nUmCcZ5RKF>. Spotlight.

Ho, J., Jain, A., and Abbeel, P. Denoising diffusion probabilistic models. In *NeurIPS*, 2020.

Iscen, A., Tolias, G., Avrithis, Y., and Chum, O. Transductive information maximization for few-shot learning. In *CVPR*, 2020.

Kang, B., Xie, Y., Rohrbach, M., Yan, Z., Gordo, A., Feng, J., and Kalantidis, Y. Decoupling representation and classifier for long-tailed recognition. In *International Conference on Learning Representations (ICLR)*, 2020.

Karras, T., Laine, S., and Aila, T. A style-based generator architecture for generative adversarial networks. In *Proceedings of the IEEE/CVF conference on computer vision and pattern recognition*, pp. 4401–4410, 2019.

Lee, H., Kim, H.-E., and Kim, J.-H. Self-supervised label augmentation via input transformations. In *Proceedings of the 37th International Conference on Machine Learning (ICML)*, 2020. SLA-AG variant (aggregation) results reported in the paper.

Lee, K., Maji, S., Ravichandran, A., and Soatto, S. Meta-learning with differentiable convex optimization. In *Proceedings of the IEEE/CVF Conference on Computer Vision and Pattern Recognition (CVPR)*, 2019.

Li, A., Huang, W., Lan, X., Feng, J., Li, Z., and Wang, L. Boosting few-shot learning with adaptive margin loss. In *Proceedings of the IEEE/CVF Conference on Computer Vision and Pattern Recognition (CVPR)*, pp. 12576–12584, 2020.

Li, Z., Zhou, F., Chen, F., and Li, H. Meta-sgd: Learning to learn quickly for few shot learning. In *NeurIPS*, 2017.

Liang, J., He, R., and Tan, T. A comprehensive survey on test-time adaptation under distribution shifts. *International Journal of Computer Vision*, 133(1):31–64, July 2024. ISSN 1573-1405. doi: 10.1007/s11263-024-02181-w. URL <http://dx.doi.org/10.1007/s11263-024-02181-w>.

Liu, H. X. and Feng, S. Curse of rarity for autonomous vehicles. *nature communications*, 15(1):4808, 2024.

Liu, M.-Y., Huang, X., Mallya, A., Karras, T., Aila, T., Lehtinen, J., and Kautz, J. Few-shot unsupervised image-to-image translation. In *arxiv*, 2019a.

Liu, Y., Lee, J., Park, M., Kim, S., Yang, E., Hwang, S. J., and Yang, Y. Learning to propagate labels: Transductive propagation network for few-shot learning. In *ICLR*, 2019b.

Liu, Z., Lin, Y., Cao, Y., Hu, H., Wei, Y., Zhang, Z., Lin, S., and Guo, B. Swin transformer: Hierarchical vision transformer using shifted windows. In *Proceedings of the IEEE/CVF International Conference on Computer Vision (ICCV)*, pp. 10012–10022, October 2021.

Meng, C., He, Y., Song, J., et al. SDEdit: Image synthesis and editing with stochastic differential equations. In *ICLR*, 2022.

Mou, C., Wang, Y., Bai, Y., et al. T2i-adapter: Learning adapters to dig out more controllable ability for text-to-image diffusion models. In *CVPR*, 2023.

Ni, R., Goldblum, M., Sharaf, A., Kong, K., and Goldstein, T. Data augmentation for meta-learning. *arXiv preprint arXiv:2010.07092*, 2020.

Nichol, A. and Dhariwal, P. Improved denoising diffusion probabilistic models. *arXiv:2102.09672*, 2021.

Nichol, A., Achiam, J., and Schulman, J. On first-order meta-learning algorithms. *arXiv:1803.02999*, 2018.

Raghu, M., Raghu, M., Bengio, S., and Vinyals, O. Rapid learning or feature reuse? towards understanding the effectiveness of maml. In *ICLR*, 2020.

Rombach, R., Blattmann, A., Lorenz, D., Esser, P., and Ommer, B. High-resolution image synthesis with latent diffusion models, 2022a.

Rombach, R., Blattmann, A., Lorenz, D., Esser, P., and Ommer, B. Stable diffusion v1.5. <https://huggingface.co/runwayml/stable-diffusion-v1-5>, 2022b. Accessed: 2025-12-04.

Ronneberger, O., Fischer, P., and Brox, T. U-net: Convolutional networks for biomedical image segmentation. In *International Conference on Medical Image Computing and Computer-Assisted Intervention (MICCAI)*, pp. 234–241. Springer, 2015.

Russakovsky, O., Deng, J., Su, H., Krause, J., Satheesh, S., Ma, S., Huang, Z., Karpathy, A., Khosla, A., Bernstein, M., Berg, A. C., and Fei-Fei, L. ImageNet Large Scale Visual Recognition Challenge. *International Journal of Computer Vision (IJCV)*, 115(3):211–252, 2015. doi: 10.1007/s11263-015-0816-y.

Schwartz, E., Karlinsky, L., Avidan, S., and Bronstein, A. M. Delta-encoder: an effective sample synthesis method for few-shot object recognition. In *NeurIPS*, 2018.

Snell, J., Swersky, K., and Zemel, R. Prototypical networks for few-shot learning. *Advances in neural information processing systems*, 30, 2017.

Sohl-Dickstein, J., Weiss, E. A., Maheswaranathan, N., and Ganguli, S. Deep unsupervised learning using nonequilibrium thermodynamics. In *ICML*, 2015.

Sung, F., Yang, Y., Zhang, L., Xiang, T., Torr, P. H., and Hospedales, T. Learning to compare: Relation network for few-shot learning. In *CVPR*, 2018.

Trabucco, B., Doherty, K., Gurinas, M. A., and Salakhutdinov, R. Effective data augmentation with diffusion models. In *Proceedings of the Twelfth International Conference on Learning Representations (ICLR)*, 2024. URL <https://openreview.net/forum?id=ZWzUA9zeAg>. Poster.

Vaswani, A., Shazeer, N., Parmar, N., Uszkoreit, J., Jones, L., Gomez, A. N., Kaiser, L., and Polosukhin, I. Attention is all you need, 2017.

Vinyals, O., Blundell, C., Lillicrap, T., Kavukcuoglu, K., and Wierstra, D. Matching networks for one shot learning. In *NeurIPS*, 2016.

Wah, C., Branson, S., Welinder, P., Perona, P., and Belongie, S. cub. Technical Report CNS-TR-2011-001, California Institute of Technology, 2011.

Wang, X., Xie, L., Dong, C., and Shan, Y. Real-esrgan: Training real-world blind super-resolution with pure synthetic data. In *International Conference on Computer Vision Workshops (ICCVW)*, 2021.

Wang, Y., Yao, Q., Kwok, J. T., and Ni, L. M. Generalizing from a few examples: A survey on few-shot learning. *ACM computing surveys (csur)*, 53(3):1–34, 2020.

Wang, Y.-X., Girshick, R., Hebert, M., and Hariharan, B. Low-shot learning from imaginary data. In *Proceedings of the IEEE conference on computer vision and pattern recognition*, pp. 7278–7286, 2018.

Xu, W., Xu, Y., Wang, H., and Tu, Z. Attentional constellation nets for few-shot learning. In *International Conference on Learning Representations (ICLR)*, 2021.

Ye, H.-J., Hu, H., Zhan, D.-C., and Sha, F. Few-shot learning via embedding adaptation with set-to-set functions. In *IEEE/CVF Conference on Computer Vision and Pattern Recognition (CVPR)*, pp. 8808–8817, 2020.

Ye, P., Zhang, H., Liu, X., et al. Ip-adapter: Text compatible image prompt adapter for text-to-image diffusion models. *arXiv:2308.06721*, 2023.

Zhang, C., Cai, Y., Lin, G., and Shen, C. Deepemd: Few-shot image classification with differentiable earth mover’s distance and structured classifiers. In *Proceedings of the IEEE/CVF conference on computer vision and pattern recognition*, pp. 12203–12213, 2020.

Zhang, L., Rao, A., and Agrawala, M. Adding conditional control to text-to-image diffusion models. *arXiv:2302.05543*, 2023.

Zheng, Z., Xu, P., Zou, X., Tang, D., Li, Z., Xi, C., Wu, P., Zou, L., Zhu, Y., Chen, M., et al. Cowclip: reducing ctr prediction model training time from 12 hours to 10 minutes on 1 gpu. In *Proceedings of the AAAI conference on artificial intelligence*, volume 37, pp. 11390–11398, 2023.

Zhou, Z.-H. *Ensemble methods: foundations and algorithms*. CRC press, 2012.

Zhu, J.-Y., Park, T., Isola, P., and Efros, A. A. Unpaired image-to-image translation using cycle-consistent adversarial networks. In *Proceedings of the IEEE international conference on computer vision*, pp. 2223–2232, 2017.

Ziko, I. M., Dolz, J., Granger, E., and Ayed, I. B. Laplacian regularized few-shot learning. In *ICML*, 2020.

## A. Proof of Proposition Risk Decomposition

Recall that  $R(g) = \frac{1}{4} \mathbb{E}[(g(x) - y)^2]$  and  $f, f_A : \mathcal{X} \rightarrow \{-1, 1\}$ ,  $\tilde{f} = \frac{1}{2}(f + f_A)$ . Since  $f^2(x) = f_A^2(x) = y^2 = 1$ ,

$$R(f) = \frac{1}{4} \mathbb{E}[(f - y)^2] = \frac{1}{4} \mathbb{E}[f^2 - 2fy + y^2] = \frac{1}{2} - \frac{1}{2} \mathbb{E}[f(x)y]. \quad (14)$$

For  $\tilde{f}$ ,

$$R(\tilde{f}) = \frac{1}{4} \mathbb{E}\left[\left(\frac{f + f_A}{2} - y\right)^2\right] = \frac{1}{16} \mathbb{E}[(f + f_A)^2] - \frac{1}{4} \mathbb{E}[(f + f_A)y] + \frac{1}{4} \mathbb{E}[y^2]. \quad (15)$$

Expanding  $(f + f_A)^2 = f^2 + 2ff_A + f_A^2$  and using  $f^2 = f_A^2 = y^2 = 1$ ,

$$R(\tilde{f}) = \frac{1}{16} \mathbb{E}[2 + 2ff_A] - \frac{1}{4} \mathbb{E}[fy + f_Ay] + \frac{1}{4} = \frac{1}{8}(1 + \mathbb{E}[f(x)f_A(x)]) - \frac{1}{4} \mathbb{E}[f(x)y] - \frac{1}{4} \mathbb{E}[f_A(x)y] + \frac{1}{4}. \quad (16)$$

Subtracting  $R(f)$  gives

$$R(\tilde{f}) - R(f) = \frac{1}{4} (\mathbb{E}[f(x)y] - \mathbb{E}[f_A(x)y]) + \frac{1}{8} (\mathbb{E}[f(x)f_A(x)] - 1). \quad (17)$$

## B. Main Theoretical Results Details

Throughout this appendix we use the pairwise reduction of Section 5.1. Each input is a query-prototype pair  $x = (q, p)$  with label  $y \in \{-1, 1\}$ . For a fixed encoder  $\Phi_\theta$  and prototype  $p$  we define the difference feature  $\Omega_\theta(x) := \Phi_\theta(q) - p$  and the Euclidean score  $g_\theta(x) := -\|\Omega_\theta(x)\|_2^2$ . The 0-1 pairwise risk of  $\theta$  is

$$R_{\text{cls}}(\theta) := \mathbb{P}(y g_\theta(x) \leq 0),$$

which coincides with the classification risk used in Section 5.3.

Where the arguments apply to generic real-valued predictors, we write  $g$  for a function in a class  $\mathcal{G}$  and specialize to the encoder score class  $\mathcal{G} = \{x \mapsto g_\theta(x) : \theta \in \Theta\}$  at the end.

### B.1. Episodic Euclidean Model and Test-Time Augmentation (details)

An  $N$ -way  $K$ -shot episode has support set  $S = \{(s_{c,k}, c) : c = 1, \dots, N, k = 1, \dots, K\}$  and query set  $Q = \{(q_j, y_j)\}_{j=1}^{n_q}$  with  $y_j \in \{1, \dots, N\}$ . A single encoder  $\Phi_\theta : \mathcal{X} \rightarrow \mathbb{R}^d$  produces features  $z_{c,k} := \Phi_\theta(s_{c,k})$  and  $z_q := \Phi_\theta(q)$ . Class prototypes and the Euclidean classifier are

$$p_c := \frac{1}{K} \sum_{k=1}^K z_{c,k}, \quad \hat{y}(q) := \arg \min_c \|\Phi_\theta(q) - p_c\|_2^2,$$

where  $p_c$  corresponds to  $p_c$  in Section 4. For analysis we reduce episodes to binary query-prototype pairs:  $x = (q, p)$  with label  $y \in \{-1, 1\}$ , where  $y = +1$  if  $p$  is the prototype of the true class of  $q$  and  $y = -1$  otherwise. We work with the difference feature  $\Omega_\theta(x) := \Phi_\theta(q) - p$  and Euclidean score  $g_\theta(x) := -\|\Omega_\theta(x)\|_2^2$ , and assume a uniform pre-augmentation radius bound

$$\|\Omega_\theta(x)\|_2 \leq r_0 \quad \text{for all } x \text{ and } \theta,$$

as in Section 5.1.

At test time, 1S-DAug uses support-side feature averaging and query-side logit averaging as described in Section 4, yielding (possibly aggregated) prototypes  $p_c$ . For the theory we only need query-side notation. Let  $A_k(q)$  be the  $k$ -th augmented view of a query  $q$  ( $k = 0, \dots, K_a$ ),  $z^{(k)}(q) := \Phi_\theta(A_k(q))$ , and  $(\alpha_k)_{k=0}^{K_a}$  convex weights with  $\sum_k \alpha_k = 1$ . We define the averaged query embedding

$$\bar{z}_{\text{qry}}(q) := \sum_{k=0}^{K_a} \alpha_k z^{(k)}(q),$$

the aggregated difference feature  $\bar{\Omega}_\theta(x) := \bar{z}_{\text{qry}}(q) - p$ , and the aggregated score  $\bar{g}_\theta(x) := -\|\bar{\Omega}_\theta(x)\|_2^2$ , where  $p$  denotes a (possibly aggregated) prototype. For squared Euclidean scores, logit averaging over per-view scores  $g_\theta^{(k)}(q, p) = -\|z^{(k)}(q) - p\|_2^2$  is equivalent (up to a class-independent constant) to using  $\bar{z}_{\text{qry}}(q)$ ; see Appendix B.3. We therefore express all bounds in terms of  $\bar{\Omega}_\theta(x)$  and  $\bar{g}_\theta(x)$ .

## B.2. Margin-based Bound and Rademacher Complexity

For a score function  $g_\theta$  and a pair  $(x, y) \sim D$  with  $y \in \{-1, 1\}$ , define the signed margin  $u_\theta(x) := y g_\theta(x)$ . Fix a margin parameter  $\rho > 0$  and the piecewise-linear margin loss

$$\tau_\rho(t) := \begin{cases} 1, & t \leq 0, \\ 1 - t/\rho, & 0 < t < \rho, \\ 0, & t \geq \rho. \end{cases}$$

The (population) margin risk and empirical margin risk on a sample  $S = \{(x_i, y_i)\}_{i=1}^m$  are

$$R_\rho(\theta) := \mathbb{E}[\tau_\rho(u_\theta(x))], \quad \widehat{R}_{S,\rho}(\theta) := \frac{1}{m} \sum_{i=1}^m \tau_\rho(y_i g_\theta(x_i)).$$

Let the empirical 0-1 pairwise risk on  $S$  be

$$\widehat{R}_{\text{cls},S}(\theta) := \frac{1}{m} \sum_{i=1}^m \mathbf{1}\{y_i g_\theta(x_i) \leq 0\}.$$

Since  $\mathbf{1}\{t \leq 0\} \leq \tau_\rho(t)$ , we have

$$R_{\text{cls}}(\theta) \leq R_\rho(\theta) \quad \text{and} \quad \widehat{R}_{\text{cls},S}(\theta) \leq \widehat{R}_{S,\rho}(\theta).$$

Let  $\mathcal{G} := \{g_\theta : \theta \in \Theta\}$  be the encoder score class. Its empirical Rademacher complexity is

$$\widehat{\mathfrak{R}}_S(\mathcal{G}) := \mathbb{E}_\sigma \left[ \sup_{g \in \mathcal{G}} \frac{1}{m} \sum_{i=1}^m \sigma_i g(x_i) \right],$$

where  $\sigma_i$  are independent Rademacher variables. A standard contraction argument with  $\tau_\rho$  yields Theorem 5.2 in the main text:

**Theorem B.1** (Restatement of Theorem 5.2). *For any  $\rho > 0$  and  $\delta > 0$ , with probability at least  $1 - \delta$  over  $S \sim D^m$ , every  $\theta$  satisfies*

$$R_{\text{cls}}(\theta) \leq \widehat{R}_{S,\rho}(\theta) + \frac{2}{\rho} \widehat{\mathfrak{R}}_S(\mathcal{G}) + \sqrt{\frac{\log(1/\delta)}{2m}}.$$

**Lemma B.2** (Rademacher complexity of the encoder score class). *Suppose each encoder  $\Phi_\theta$  is realised by a feedforward network with 1-Lipschitz nonlinearities and layer spectral norms  $\|W_\ell\|_2 \leq s_\ell$  such that  $\prod_{\ell=1}^L s_\ell \leq L_{\text{enc}}$ , and that  $\|\Omega_\theta(x)\|_2 \leq r$  for all  $x$  and  $\theta$ . Then there exists a constant  $C_{\text{enc}} > 0$  (depending only on the architecture) such that, for any sample  $S$ ,*

$$\widehat{\mathfrak{R}}_S(\mathcal{G}) \leq C_{\text{enc}} L_{\text{enc}} \frac{r}{\sqrt{m}}.$$

*In particular, in the setting of Section 5.3, one may take  $r = r_0$  before augmentation and  $r = \hat{r}$  after augmentation.*

*Proof sketch.* By assumption, each encoder  $\Phi_\theta$  is realised by a feedforward network with 1-Lipschitz nonlinearities and layer spectral norms  $\|W_\ell\|_2 \leq s_\ell$  satisfying  $\prod_{\ell=1}^L s_\ell \leq L_{\text{enc}}$ . Standard results on spectral-norm control of deep networks (e.g. via composing linear maps and 1-Lipschitz activations) imply that  $\Phi_\theta$  is  $L_{\text{enc}}$ -Lipschitz with respect to the input  $\ell_2$ -norm, i.e.

$$\|\Phi_\theta(x) - \Phi_\theta(x')\|_2 \leq L_{\text{enc}} \|x - x'\|_2 \quad \text{for all } x, x'.$$

Since  $p$  does not depend on  $q$  for a fixed pair  $x = (q, p)$ , the difference feature  $\Omega_\theta(x) = \Phi_\theta(q) - p$  is also  $L_{\text{enc}}$ -Lipschitz in  $q$ . On the domain where  $\|\Omega_\theta(x)\|_2 \leq r$  for all  $x$  and  $\theta$ , the score  $g_\theta(x) = -\|\Omega_\theta(x)\|_2^2$  is  $2rL_{\text{enc}}$ -Lipschitz in  $x$ : the gradient of  $g_\theta$  with respect to  $\Omega_\theta$  has norm  $2\|\Omega_\theta(x)\|_2 \leq 2r$ , and  $\Omega_\theta$  itself is  $L_{\text{enc}}$ -Lipschitz.

Let  $\mathcal{G} = \{g_\theta : \theta \in \Theta\}$  be the corresponding score class. It is therefore contained in a class of Lipschitz real-valued functions whose Lipschitz constant is bounded by  $2rL_{\text{enc}}$ . Standard covering-number/Rademacher arguments for such Lipschitz

function classes (see, e.g., generic chaining bounds for  $L$ -Lipschitz functions on an  $\ell_2$ -ball) yield that there exists a constant  $C > 0$ , depending only on the input dimension and hence only on the architecture, such that for any sample  $S$  of size  $m$ ,

$$\widehat{\mathfrak{R}}_S(\mathcal{G}) \leq C (2rL_{\text{enc}}) \frac{1}{\sqrt{m}}.$$

Setting  $C_{\text{enc}} := 2C$  gives

$$\widehat{\mathfrak{R}}_S(\mathcal{G}) \leq C_{\text{enc}} L_{\text{enc}} \frac{r}{\sqrt{m}},$$

which is the claimed bound.  $\square$

### B.3. Equivalence of Logit Averaging and Feature Averaging

For completeness we record the standard equivalence between logit averaging and feature averaging for squared Euclidean scores.

Fix a query  $q$  and a prototype  $p$ , and let

$$z^{(k)}(q) := \Phi_\theta(A_k(q))$$

denote the encoded query under augmentation  $k$ , with convex weights  $\alpha_k \geq 0$ ,  $\sum_k \alpha_k = 1$ . The per-view scores are

$$g_\theta^{(k)}(q, p) := -\|z^{(k)}(q) - p\|_2^2, \quad \tilde{g}_\theta(q, p) := \sum_k \alpha_k g_\theta^{(k)}(q, p).$$

Define the averaged query feature

$$\bar{z}(q) := \sum_k \alpha_k z^{(k)}(q), \quad g_\theta^{\text{avg}}(q, p) := -\|\bar{z}(q) - p\|_2^2.$$

Then

$$\begin{aligned} \tilde{g}_\theta(q, p) &= -\sum_k \alpha_k \|z^{(k)}(q) - p\|_2^2 \\ &= -\sum_k \alpha_k \left( \|z^{(k)}(q)\|_2^2 - 2\langle z^{(k)}(q), p \rangle + \|p\|_2^2 \right) \\ &= -\sum_k \alpha_k \|z^{(k)}(q)\|_2^2 + 2 \left\langle \sum_k \alpha_k z^{(k)}(q), p \right\rangle - \|p\|_2^2 \\ &= -\sum_k \alpha_k \|z^{(k)}(q)\|_2^2 - \|\bar{z}(q)\|_2^2 + \|\bar{z}(q)\|_2^2 + 2 \langle \bar{z}(q), p \rangle - \|p\|_2^2 \\ &= -\|\bar{z}(q) - p\|_2^2 - \sum_k \alpha_k \|z^{(k)}(q)\|_2^2 + \|\bar{z}(q)\|_2^2. \end{aligned}$$

The last two terms depend on  $q$  and the set of views  $\{z^{(k)}(q)\}$  but not on  $p$ . Hence, for fixed  $q$ , comparing classes by  $\tilde{g}_\theta(q, p_c)$  is equivalent to comparing them by

$$g_\theta^{\text{avg}}(q, p_c) = -\|\bar{z}(q) - p_c\|_2^2.$$

In other words, query-side logit averaging with squared Euclidean scores induces exactly the same class ranking as nearest-prototype classification in the feature space of the averaged query embedding  $\bar{z}(q)$ .

This justifies working, for analysis, with the aggregated difference feature

$$\bar{\Omega}_\theta(x) := \bar{z}(q) - p$$

and its radius, even though the implementation performs logit averaging rather than explicit feature averaging on the query side.

#### B.4. Stability of the Empirical Margin Risk

Let  $S = \{(x_i, y_i)\}_{i=1}^m$  be the original sample and let  $\widehat{S}$  denote the same pairs  $(x_i, y_i)$  but with the empirical margin risk evaluated using the aggregated difference features  $\widehat{\Omega}_\theta(x_i)$ . Write

$$\Omega_i := \Omega_\theta(x_i), \quad \widehat{\Omega}_i := \widehat{\Omega}_\theta(x_i),$$

and recall that  $g_\theta(x) = -\|\Omega_\theta(x)\|_2^2$ . Abusing notation slightly, we write  $g_\theta(\Omega)$  for the score evaluated at a difference feature  $\Omega$ , i.e.  $g_\theta(\Omega) := -\|\Omega\|_2^2$ . Assume that  $g_\theta(\cdot)$  is  $L_g$ -Lipschitz with respect to its feature argument on the radius- $r_0$  ball in  $\mathbb{R}^d$ .

**Lemma B.3** (Empirical margin stability). *For any  $\rho > 0$ ,*

$$|\widehat{R}_{\widehat{S}, \rho}(\theta) - \widehat{R}_{S, \rho}(\theta)| \leq \frac{L_g}{\rho m} \sum_{i=1}^m \|\widehat{\Omega}_i - \Omega_i\|_2. \quad (18)$$

In particular,

$$|\widehat{R}_{\widehat{S}, \rho}(\theta) - \widehat{R}_{S, \rho}(\theta)| \leq \frac{L_g}{\rho} \cdot \left( \frac{1}{m} \sum_{i=1}^m \|\widehat{\Omega}_i - \Omega_i\|_2 \right). \quad (19)$$

*Proof.* For each  $i$ ,

$$|\tau_\rho(y_i g_\theta(\widehat{\Omega}_i)) - \tau_\rho(y_i g_\theta(\Omega_i))| \leq \frac{1}{\rho} |y_i g_\theta(\widehat{\Omega}_i) - y_i g_\theta(\Omega_i)| = \frac{1}{\rho} |g_\theta(\widehat{\Omega}_i) - g_\theta(\Omega_i)|.$$

Since  $g_\theta$  is  $L_g$ -Lipschitz in its feature argument,

$$|g_\theta(\widehat{\Omega}_i) - g_\theta(\Omega_i)| \leq L_g \|\widehat{\Omega}_i - \Omega_i\|_2.$$

Combining the two displays gives

$$|\tau_\rho(y_i g_\theta(\widehat{\Omega}_i)) - \tau_\rho(y_i g_\theta(\Omega_i))| \leq \frac{L_g}{\rho} \|\widehat{\Omega}_i - \Omega_i\|_2.$$

Averaging over  $i$  and using the triangle inequality yields (18).  $\square$

For the Euclidean score class considered here we can take  $L_g \leq 2r_0$ , since  $z \mapsto -\|z\|_2^2$  has gradient of norm  $2\|z\|_2$  and is therefore  $2r_0$ -Lipschitz on the radius- $r_0$  ball.

#### B.5. Probabilistic Radius Reduction with Multiple Augmentations

For each  $i = 1, \dots, m$  and  $k = 0, \dots, M$ , let  $\{\Omega_i^{(k)} \in \mathbb{R}^d\}$  be i.i.d. feature vectors with radii  $R_i^{(k)} := \|\Omega_i^{(k)}\|_2$ . Define

$$R_{\text{orig}}^{\max} := \max_{1 \leq i \leq m} R_i^{(0)}, \quad R_{\text{aug}}^{\max} := \max_{1 \leq i \leq m} \max_{1 \leq k \leq M} R_i^{(k)}. \quad (20)$$

Define the aggregated feature and corresponding radii

$$\widehat{\Omega}_i := \frac{1}{M+1} \sum_{k=0}^M \Omega_i^{(k)}, \quad \widehat{R}_i := \|\widehat{\Omega}_i\|_2, \quad \widehat{R}^{\max} := \max_{1 \leq i \leq m} \widehat{R}_i. \quad (21)$$

**Proposition B.4** (Radius reduction with  $M$  augmentations). *Assume  $\{\Omega_i^{(k)}\}_{i,k}$  are i.i.d. from a continuous distribution on  $\mathbb{R}^d$ . Then*

$$\mathbb{P}(\widehat{R}^{\max} < R_{\text{orig}}^{\max}) \geq \mathbb{P}(R_{\text{aug}}^{\max} < R_{\text{orig}}^{\max}) = \frac{1}{M+1}. \quad (22)$$

*Proof.* Consider all  $m(M+1)$  radii  $\{R_i^{(k)}\}_{i,k}$ , which are i.i.d. on  $\mathbb{R}_+$ . Let  $R_{\text{all}}^{\max} := \max_{i,k} R_i^{(k)}$ . By continuity, this maximum is almost surely unique and, by symmetry, each of the  $m(M+1)$  radii is equally likely to be the maximum. The event  $\{R_{\text{aug}}^{\max} < R_{\text{orig}}^{\max}\}$  occurs exactly when the unique maximum lies among the  $m$  original radii  $\{R_i^{(0)}\}$ , hence

$$\mathbb{P}(R_{\text{aug}}^{\max} < R_{\text{orig}}^{\max}) = \frac{m}{m(M+1)} = \frac{1}{M+1}.$$

Now fix an outcome in this event. Let  $I$  be the (unique) index such that  $R_I^{(0)} = R_{\text{orig}}^{\max}$ . Then for every  $i$  and  $k \geq 1$ ,  $R_i^{(k)} < R_{\text{orig}}^{\max}$ , and for all  $j \neq I$ ,  $R_j^{(0)} < R_{\text{orig}}^{\max}$ . For  $i = I$ , the average of the  $M + 1$  vectors  $\{\Omega_I^{(k)}\}$  has strictly smaller norm than the largest of them: not all  $\Omega_I^{(k)}$  are equal (by continuity), and the Euclidean norm is strictly convex, so

$$\hat{R}_I = \left\| \frac{1}{M+1} \sum_{k=0}^M \Omega_I^{(k)} \right\|_2 < R_{\text{orig}}^{\max}.$$

For any  $j \neq I$ , each  $\|\Omega_j^{(k)}\|_2$  is strictly less than  $R_{\text{orig}}^{\max}$ , hence by the triangle inequality

$$\hat{R}_j = \left\| \frac{1}{M+1} \sum_{k=0}^M \Omega_j^{(k)} \right\|_2 \leq \frac{1}{M+1} \sum_{k=0}^M \|\Omega_j^{(k)}\|_2 < R_{\text{orig}}^{\max}.$$

Thus  $\hat{R}^{\max} < R_{\text{orig}}^{\max}$  on this event, so

$$\mathbb{P}(\hat{R}^{\max} < R_{\text{orig}}^{\max}) \geq \mathbb{P}(R_{\text{aug}}^{\max} < R_{\text{orig}}^{\max}) = \frac{1}{M+1}.$$

□

## B.6. Training-time versus Test-time Augmentation

Let  $P_{\text{base}}$  and  $P_{\text{novel}}$  denote the base and novel pairwise distributions on  $(x, y)$ , and let the corresponding 0-1 pairwise risks for the encoder score  $g_\theta$  be

$$R_{\text{base}}(\theta) := \mathbb{P}_{(x,y) \sim P_{\text{base}}}(y g_\theta(x) \leq 0), \quad R_{\text{novel}}(\theta) := \mathbb{P}_{(x,y) \sim P_{\text{novel}}}(y g_\theta(x) \leq 0).$$

**Training-time augmentation on base classes.** Let

$$S_{\text{base}} = \{(x_i, y_i)\}_{i=1}^{m_{\text{base}}} \sim P_{\text{base}}^{m_{\text{base}}}. \quad (23)$$

At training time, generate  $M_{\text{tr}}$  augmentations per example:

$$x_i^{(0)} = x_i, \quad x_i^{(k)} = A_k^{\text{tr}}(x_i), \quad k = 1, \dots, M_{\text{tr}}, \quad (24)$$

with difference features  $\Omega_\theta(x_i^{(k)})$ . Assume a radius bound

$$\|\Omega_\theta(x_i^{(k)})\|_2 \leq r_{0,\text{base}}^{\text{aug}} \quad \text{for all } i, k.$$

The augmented training sample is

$$S_{\text{base}}^{\text{tr-aug}} = \{(x_i^{(k)}, y_i) : i = 1, \dots, m_{\text{base}}, k = 0, \dots, M_{\text{tr}}\}, \quad (25)$$

of size  $m_{\text{base}}(M_{\text{tr}} + 1)$ .

**Proposition B.5** (Training-time augmentation bound on base distribution). *Under the assumptions above, there exists  $C_{\text{enc}} > 0$  (as in Lemma B.2) such that for any  $\rho > 0$  and  $\delta > 0$ , with probability at least  $1 - \delta$  over  $S_{\text{base}} \sim P_{\text{base}}^{m_{\text{base}}}$ , every encoder  $\theta$  satisfies*

$$R_{\text{base}}(\theta) \leq \hat{R}_{S_{\text{base}}^{\text{tr-aug}}, \rho}(\theta) + \frac{2C_{\text{enc}}L_{\text{enc}}}{\rho} \frac{r_{0,\text{base}}^{\text{aug}}}{\sqrt{m_{\text{base}}(M_{\text{tr}} + 1)}} + \sqrt{\frac{\log(1/\delta)}{2m_{\text{base}}(M_{\text{tr}} + 1)}}. \quad (26)$$

*Proof.* Apply Theorem 5.2 to the score class  $\mathcal{G}$  on the augmented sample  $S_{\text{base}}^{\text{tr-aug}}$ , with sample size  $m_{\text{base}}(M_{\text{tr}} + 1)$  and radius parameter  $r_{0,\text{base}}^{\text{aug}}$ . Lemma B.2 bounds the empirical Rademacher complexity by  $C_{\text{enc}}L_{\text{enc}}r_{0,\text{base}}^{\text{aug}}/\sqrt{m_{\text{base}}(M_{\text{tr}} + 1)}$ , yielding (26). □

To relate base and novel risks, assume there exists a discrepancy functional  $\text{disc}_{\mathcal{G}}$  such that for all encoders  $\theta$ ,

$$R_{\text{novel}}(\theta) \leq R_{\text{base}}(\theta) + \text{disc}_{\mathcal{G}}(P_{\text{base}}, P_{\text{novel}}). \quad (27)$$

Combining (27) with Proposition B.5 upper-bounds  $R_{\text{novel}}(\theta)$  via a term controlled by training-time augmentation on  $P_{\text{base}}$  plus the discrepancy.

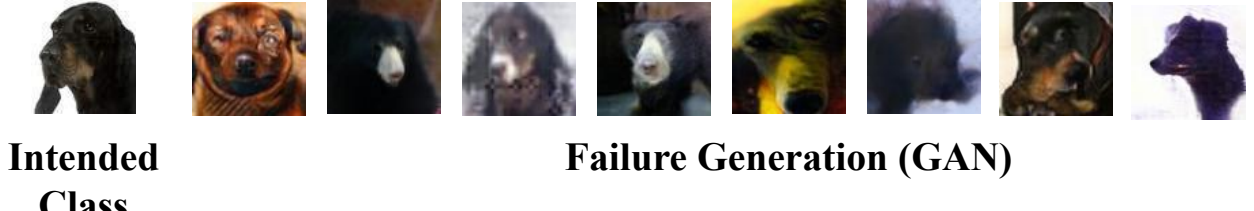


Figure 4. Failure modes of GAN-based image-to-image translation. Examples where image-to-image GAN translation fails to preserve the intended class. Rows contain target class and failed GAN outputs with typical artifacts.

**Test-time augmentation on novel classes.** For the novel distribution, consider a labeled sample

$$S_{\text{novel}} = \{(x_i, y_i)\}_{i=1}^{m_{\text{novel}}} \sim P_{\text{novel}}^{m_{\text{novel}}}. \quad (28)$$

At test time, generate  $M$  augmentations per example, form aggregated difference features  $\widehat{\Omega}_\theta(x_i)$ , and let  $\widehat{S}_{\text{novel}}$  denote the sample with these aggregated features. Let  $\widehat{r}_{\text{novel}}$  be a radius bound for the aggregated novel features, i.e.,

$$\|\widehat{\Omega}_\theta(x_i)\|_2 \leq \widehat{r}_{\text{novel}} \quad \text{for all } i.$$

Applying Theorem 5.2 and Lemma B.2 directly to  $\widehat{S}_{\text{novel}}$  yields, with probability at least  $1 - \delta$ ,

$$R_{\text{novel}}(\theta) \leq \widehat{R}_{\widehat{S}_{\text{novel}}, \rho}(\theta) + \frac{2C_{\text{enc}}L_{\text{enc}}}{\rho} \frac{\widehat{r}_{\text{novel}}}{\sqrt{m_{\text{novel}}}} + \sqrt{\frac{\log(1/\delta)}{2m_{\text{novel}}}}. \quad (29)$$

Proposition B.4 shows that, in an idealized i.i.d. model with  $M$  augmentations per example, the maximum radius of novel features decreases after augmentation with probability at least  $1/(M + 1)$ , which in turn tends to reduce  $\widehat{r}_{\text{novel}}$  relative to the original radius bound. Besides, assuming that the aggregated samples become closer to the typical prototype (Bai et al., 2025), and considering Lemma B.3, we have test-time augmentation shrink the complexity term and reduce the empirical margin risk on the target distribution  $P_{\text{novel}}$  itself.

In contrast, training-time augmentation mainly tightens the bound on  $R_{\text{base}}(\theta)$ ; any bound on  $R_{\text{novel}}(\theta)$  obtained via (27) still contains the discrepancy  $\text{disc}_{\mathcal{G}}(P_{\text{base}}, P_{\text{novel}})$ , which can be large when base and novel classes differ substantially. This highlights the comparative advantage of test-time augmentation for few-shot generalisation under distribution shift.

## C. Efficiency

Table 6. Per-image generation time across noise levels. Higher noise entails more denoising compute. Measured on a single GPU; see experimental setup for hardware details.

	0.25 Noise	0.50 Noise	0.75 Noise	1.00 Noise
Generation Time (s) ↓	0.41	0.68	0.92	1.42

We record the wall-clock running time for our inference script, and the results are reported in Table 6. All experiments are run on a single NVIDIA RTX A5000 GPU. As expected, runtime scales with the noising level. Higher noising produces larger edits and requires longer inference, whereas lower noising is faster. As we start from the noisy image halfway, the inference cost is generally lower than that of standard diffusion process starting from pure noise.

## D. GAN Failure Case Illustration

Figure 4 illustrates the failure cases of GAN-based image-to-image translation models (Liu et al., 2019a).

## E. More Implementation Details

### E.1. FSL model training (ProtoNet and FEAT)

We follow the public FEAT repository for episodic training and evaluation, including 5-way, 1-shot meta-training; 15 queries/class for both train and evaluation; Euclidean distance for classification; Res12 as the default backbone. Key arguments (defaults shown where applicable) are exposed by `train_fsl.py`: *task setup* {dataset={miniImagenet, tieredImageNet, CUB, Animals}, way=5, shot=1, query=15; eval\_way=5, eval\_shot=1, eval\_query=15}; *optimization* {max\_epoch=400, episodes\_per\_epoch=100, num\_eval\_episodes=200, lr =  $10^{-4}$  (with pre-trained weights), lr\_scheduler=step, step\_size=20, gamma=0.2, momentum=0.9, weight\_decay =  $5 \cdot 10^{-4}$ }; *model* {model.class ∈ {ProtoNet, FEAT}, backbone\_class ∈ {ConvNet, Res12}, use\_euclidean (Euclidean distances), temperature=1 (ProtoNet)/64 (FEAT), lr\_mul=10 for the set-to-set head}. Example FEAT commands for Res12 on tieredImageNet use lr =  $2 \cdot 10^{-4}$ , step\_size ∈ {20, 40},  $\gamma$  = 0.5, and temperatures temperature = 64, temperature2 ∈ {64, 32}; we mirror this recipe for our FEAT runs and use the same episodic protocol for ProtoNet.

Concretely, in our re-trains we use:

- **Backbones:** Res12 (all models except CUB), ConvNet (CUB).
- **ProtoNet:** model.class = ProtoNet, Euclidean distances, max\_epoch = 400, episodes\_per\_epoch = 100, lr = 1e-4 (pretrained), step scheduler with step\_size = 20,  $\gamma$  = 0.2; temperature = 1 unless otherwise tuned on validation; momentum = 0.9, weight\_decay =  $5 \cdot 10^{-4}$ . (All other task/eval counts as above.)
- **FEAT:** model.class = FEAT, lr = 2e-4, lr\_mul = 10 for the Transformer head, step scheduler with step\_size in {20, 40} and  $\gamma$  = 0.5; temperature = 64, temperature2 ∈ {64, 32}; Euclidean distances enabled; same episodic counts as ProtoNet.

At evaluation, we sample 15,000 queries and report mean accuracy with 95% confidence intervals, matching the repository’s evaluation practice.

### E.2. 1S-DAug (one-shot test-time augmentation) configuration

We implement 1S-DAug as an image-conditioned denoising pipeline and a light, class-preserving geometric pre-edit (“shape tweak”). The script exposes the following arguments (defaults in ·), which we fix across all main tables unless the ablation states otherwise:

**Core diffusion/editing.** We use stable-diffusion-v1.5 from the diffusers library as the base image generator.  $-\text{noise-level} \in [0, 1] \cdot 0.7$ : entry point on the diffusion trajectory (larger = more rewrite, smaller = higher faithfulness);  $-\text{steps} \cdot 20$ : denoising steps;  $-\text{cfg} \cdot 9.0$ : guidance scale;  $-\text{seed}$  for deterministic replication; attention slicing is enabled; VAE tiling can be toggled for large images.

**Backbone generator.**  $-\text{model} \cdot \text{runwayml/stable-diffusion-v1-5}$ ; images are fed at  $512 \times 512$  resolution. Benchmarks originally at  $84 \times 84$  are upsampled before augmentation using Real-ESRGAN (Wang et al., 2021).

**Image-prompt adapter (optional).**  $-\text{ip\_adapter}$  (on/off),  $-\text{ip\_repo} \cdot \text{h94/IP-Adapter}$ ,  $-\text{ip\_scale} \cdot 0.8$  controls conditioning strength.

**Shape tweaking (geometric seed).** Enabled via  $-\text{shape\_aug}$ ; parameters:  $-\text{shape-aug-rotate} \cdot 20^\circ$  (uniform in  $[-R, +R]$ );  $-\text{shape-aug-stretch} \cdot 0.20$  (anisotropic scales  $s_x, s_y \in [1 - S, 1 + S]$ );  $-\text{shape-aug-translate} \cdot 0.025$  (fraction of width/height);  $-\text{shape-aug-persp} \cdot 0.12$  (corner jitter fraction for a single-view projective warp). Intermediate augmented images can be saved for inspection with  $-\text{save\_aug}$ .

**I/O and batching.** Single-image mode or directory batch mode; recursive directory traversal and extension override are supported; per-image runtime and peak memory are logged (used in our efficiency table).

**Recommended ranges (used in ablations).** Noise levels  $\in \{0.25, 0.5, 0.75, 1.0\}$ ; shape tweaks at the defaults above or slightly weaker for fine-grained datasets. When noise is very small, diversity is limited; when very large, fidelity drops unless image conditioning is active (consistent with our qualitative/quantitative ablations).

## F. More Related Work

**Few-shot Learning.** FSL methods commonly fall into metric-, model-, and augmentation-based families. *Metric-based* methods learn an embedding where queries are classified by proximity to supports or class prototypes, including Matching Networks (Vinyals et al., 2016), Prototypical Networks (Snell et al., 2017), Relation Networks (Sung et al., 2018), and episodic feature adaptation such as FEAT (Ye et al., 2020). Strong baselines refine this recipe with improved training protocols and heads, e.g., Baseline++ (Chen et al., 2019), Meta-Baseline (Chen et al., 2021), MetaOptNet (Lee et al., 2019), and transductive inference methods such as TPN (Liu et al., 2019b), LaplacianShot (Ziko et al., 2020), and TIM (Iscen et al., 2020). *Model-based* approaches emphasize rapid parameter adaptation from few examples, e.g., gradient-based meta-learning with MAML (Finn et al., 2017), Meta-SGD (Li et al., 2017), Reptile (Nichol et al., 2018), and ANIL (Raghu et al., 2020). *Augmentation-based* approaches increase training diversity via feature or image synthesis—e.g., feature hallucination (Hariharan & Girshick, 2017b) and delta-based example synthesizers (Schwartz et al., 2018). These are primarily *training-time* techniques that rely on base-class supervision; by contrast, few-shot *test-time* augmentation must produce high-quality, class-faithful variants for unseen classes without retraining or labels.

Test-time generative augmentation for FSL remains limited. Bai et al. (2025) uses an adversarial image-to-image translator to combine the geometric “shape” of one image with the class-defining “style” of another (i.e., FUNIT (Liu et al., 2019a)) for inference-time augmentation. While a useful proof of concept, the dataset scope is narrow and failure arises on more complex, diverse categories, reflecting the difficulty of preserving content under large structural gaps.

**Diffusion Models.** Early diffusion models established iterative denoising as a competitive generative paradigm (Sohl-Dickstein et al., 2015; Ho et al., 2020), with subsequent improvements to training and sampling (Nichol & Dhariwal, 2021). Latent-space diffusion amortizes computation via a learned autoencoder, enabling high-resolution synthesis (Rombach et al., 2022a). Attention-based conditioning adapters inject external signals into cross-attention without retraining the denoiser, supporting controllable editing and image-conditioned generation, including image-prompt adapters (Ye et al., 2023), general adapters (Mou et al., 2023), and control modules such as ControlNet (Zhang et al., 2023). These advances in stability, controllability, and fidelity make diffusion well-suited for few-shot test-time augmentation. Editing-by-denoising constructs variants by adding controlled noise to a source image and running the reverse process with conditioning (Meng et al., 2022). However, in this setup, too little noise yields small changes, and too much sacrifices faithfulness (e.g., changes object type), which is not suitable for data augmentation.

**GAN/Diffusion-based Data Augmentation.** Adversarial generators have long been used for data expansion and translation. Few-shot translation frameworks (e.g., FUNIT (Liu et al., 2019a) and derivatives), unpaired mappers (CycleGAN (Zhu et al., 2017)), and class-conditional generators (StyleGAN families (Karras et al., 2019)) can expand training sets but face limitations for FSL test-time augmentation, including training stability, mode coverage, and faithfulness for *unseen* classes without supervision. For diffusion-based generators, there have been a few recent works focusing on using the diffusion-based synthetic images for downstream tasks other than few-shot learning. However, these works rely on fine-tuning with text prompts or a handful of extra target-class samples, not suitable for test-time augmentation (He et al., 2023; Benigmim et al., 2023). In contrast, we do not rely on any label or additional target-class samples, and the strict set-up fulfills the requirement for challenging downstream tasks like FSL test-time augmentation.

## G. Algorithm Summary

Algorithmic summary of 1SDAug is available as Algorithm 1.

## H. Use of Large Language Models

**Writing assistance.** Yes—large language models (LLMs) were used to aid and polish writing (e.g., improving clarity, tightening tone, harmonizing notation, and converting prose to L<sup>A</sup>T<sub>E</sub>X). Substantive technical content, mathematical formulations, and experimental design were authored by the authors; LLM outputs were treated as drafts and were edited for

**Algorithm 1** 1S-DAug (Single image  $x$ )

---

**Require:** image  $x$ ; steps  $T$ ; schedule  $(\beta_t)$ ; user noise  $\eta \in [0, 1]$ ; conditioning weight  $\lambda_{\text{img}}$ ; number of variants  $K$ ;

- 1: **Geometric seed:** sample a shape tweak  $T_\psi$  and set  $x_{\text{geom}} \leftarrow T_\psi(x)$
- 2: **Noising entry:** compute  $t_0$  from  $\eta$  via equation (2); draw  $x_{t_0} \sim q(\cdot \mid x_{\text{geom}})$  using equation (1)
- 3: **Working state:** set  $z_{t_0} \leftarrow x_{t_0}$  (pixel space) or  $z_{t_0} \leftarrow \text{Enc}(x_{t_0})$  (latent variant)
- 4: **for**  $k = 1$  **to**  $K$  **do**
- 5:   **for**  $t = t_0, t_0 - 1, \dots, 1$  **do**
- 6:     Form  $K_t, V_t$  by equation (7) using  $x$  (and  $p$  if used); set  $Q_t = W_Q z_t$  and compute  $c_t \leftarrow A_t(Q_t, K_t, V_t)$
- 7:     **Reverse step:** update  $z_{t-1} \leftarrow \mu_\varphi(z_t, t, c_t) + \sigma_t \epsilon$  via equation (3), with  $\epsilon \sim \mathcal{N}(0, I)$
- 8:   **end for**
- 9:   **Decode:**  $\tilde{x}^{(k)} \leftarrow \text{Dec}(z_0)$  {identity if denoising in pixel space}
- 10: **end for** **Return**  $\{\tilde{x}^{(k)}\}_{k=1}^K$

---

accuracy and consistency with our contributions. No text was accepted without human verification.

**Retrieval and discovery.** Yes—LLMs were used for literature discovery and organization (e.g., surfacing related work candidates, clustering themes, and drafting citation lists). All citations included in the paper were validated by the authors against the original sources; bibliographic metadata and claims were cross-checked manually. LLMs were not used to generate experimental results or to fabricate evidence.

**Scope and safeguards.** LLMs were not used to generate, alter, or select experimental data; to tune hyperparameters automatically; or to produce figures or tables beyond cosmetic wording. All code and analyses were implemented and executed by the authors, and all numbers reported in the paper come from our runs. Prompts contained only non-sensitive project information and public references, and no proprietary or personally identifying data were included. Where LLM-assisted text appears (e.g., phrasing of method and related-work passages), it was reviewed for factual faithfulness and edited for technical precision.

## I. Reproducibility Statement.

We take reproducibility seriously. The paper specifies the method mathematically (Section § 4), the experimental set-up (encoders, classifier, datasets, and episodic protocol), and all evaluation details (Section § 6); ablations and qualitative analyses are provided to validate design choices. The Appendix E details data preprocessing (including upscaling and shape-tweak parameters), hyperparameters (noise level, conditioning strength, denoising steps), and the exact episodic sampling procedure (5-way-1-shot, 15,000 queries, 95% confidence intervals). Upon paper acceptance, we will release a repository containing: training scripts for ProtoNet/FEAT under the stated backbones, inference scripts for our augmentation, configuration files for table, deterministic seeds, and instructions to download datasets and reproduce numbers end-to-end on a single GPU (the hardware we report). Where we use pretrained weights or models, we provide pointers or scripts to obtain them. Together, these materials enable exact regeneration of all reported tables and figures.

## J. 1S-DAug Visualization

Figure 5 and Figure 6 illustrate more image generation results of our proposed method.

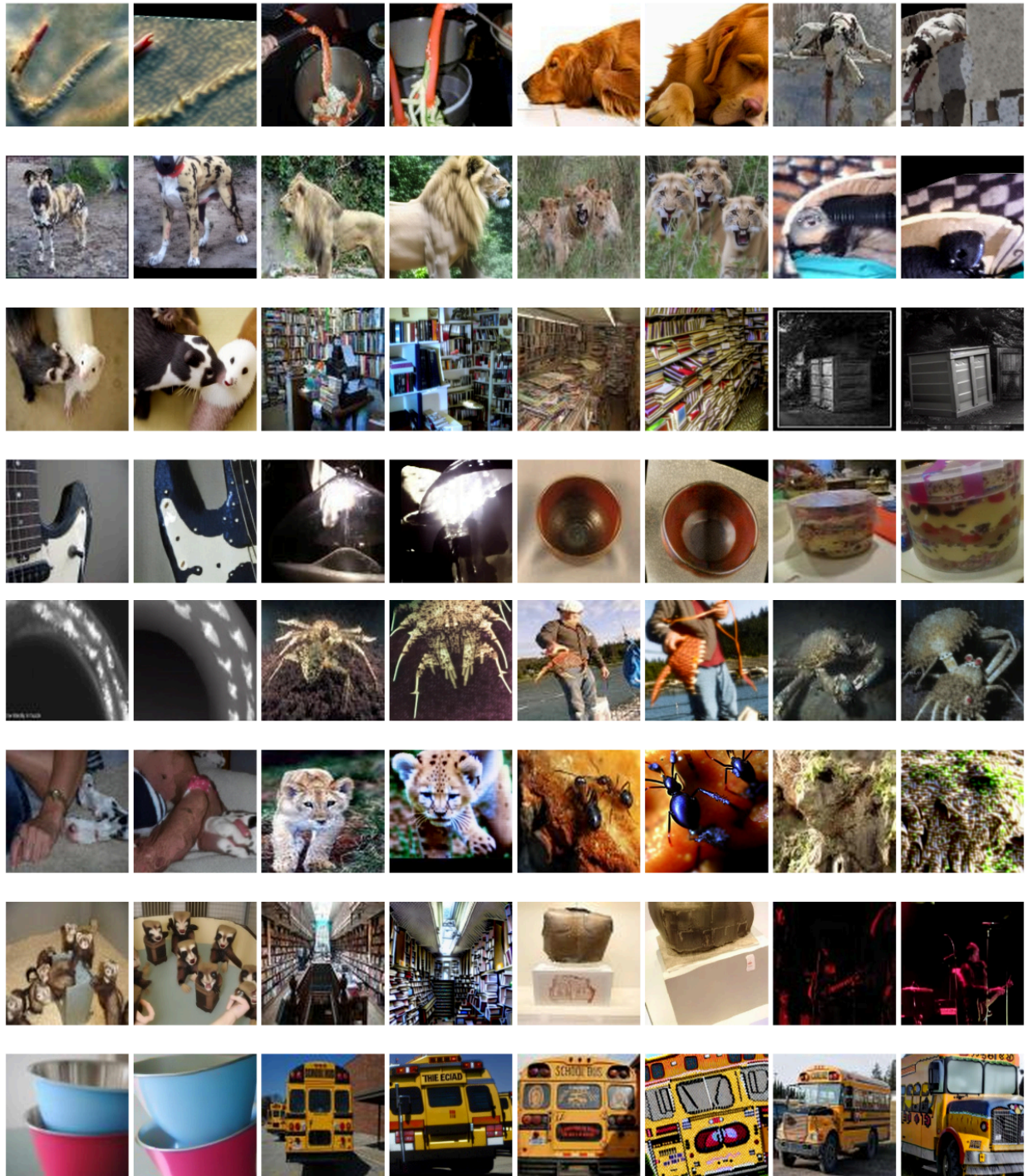


Figure 5. More qualitative results from 1S-DAug. Each pair contains the original image followed by our synthesis. All visualization pairs are random without cherry-picking.

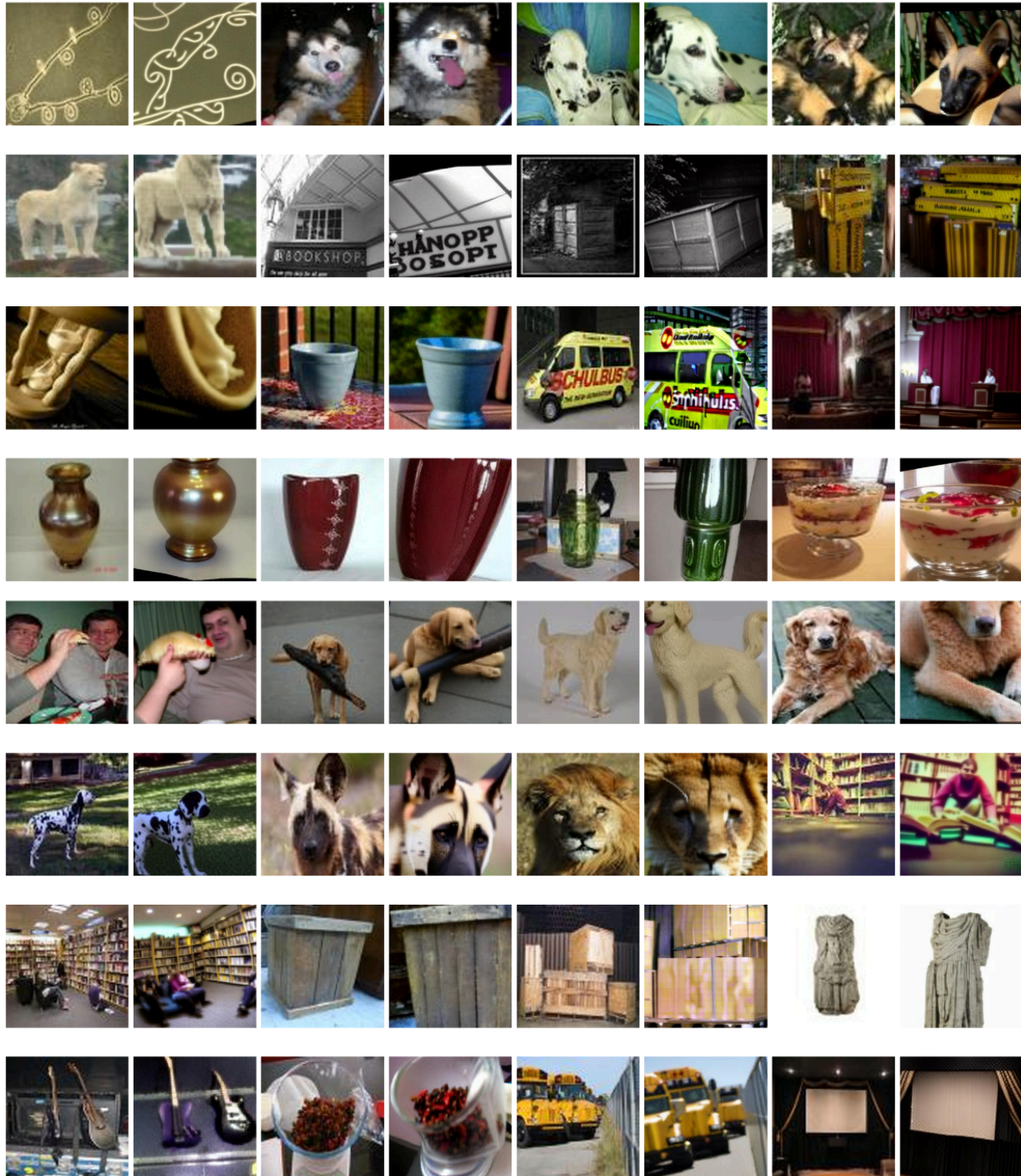


Figure 6. More qualitative results from 1S-DAug. Each pair contains the original image followed by our synthesis. All visualization pairs are random without cherry-picking.